The Astrophysical Journal Supplement Series, 242:25 (31pp), 2019 June https://doi.org/10.3847/1538-4365/ab1b16

Search for Nearby Earth Analogs. I. 15 Planet Candidates Found in PFS Data*

Fabo Feng[1], Jeffrey D. Crane[2], Sharon Xuesong Wang[1], Johanna K. Teske[1,2,5], Stephen A. Shectman[2], Matías R. Díaz[2,3], Ian B. Thompson[2], Hugh R. A. Jones[4], and R. Paul Butler[1]
[1] Department of Terrestrial Magnetism, Carnegie Institute of Washington, Washington, DC 20015, USA; ffeng@carnegiescience.edu
[2] Observatories of the Carnegie Institution for Science, 813 Santa Barbara St., Pasadena, CA 91101, USA
[3] Departamento de Astronomía, Universidad de Chile, Camino El Observatorio 1515, Las Condes, Santiago, Chile
[4] Centre for Astrophysics Research, University of Hertfordshire, College Ln., AL10 9AB, Hatfield, UK
Received 2019 March 11; revised 2019 April 9; accepted 2019 April 17; published 2019 June 17

Abstract

The radial velocity (RV) method plays a major role in the discovery of nearby exoplanets. To efficiently find planet candidates from the data obtained in high-precision RV surveys, we apply a signal diagnostic framework to detect RV signals that are statistically significant, consistent in time, robust in the choice of noise models, and do not correlated with stellar activity. Based on the application of this approach to the survey data of the Planet Finder Spectrograph, we report 15 planet candidates located in 14 stellar systems. We find that the orbits of the planet candidates around HD 210193, 103949, 8326, and 71135 are consistent with temperate zones around these stars (where liquid water could exist on the surface). With periods of 7.76 and 15.14 days, respectively, the planet candidates around star HIP 54373 form a 1:2 resonance system. These discoveries demonstrate the feasibility of automated detection of exoplanets from large RV surveys, which may provide a complete sample of nearby Earth analogs.

Key words: instrumentation: spectrographs – methods: numerical – planets and satellites: general – stars: activity – techniques: radial velocities

1. Introduction

One of the ultimate goals of exoplanet research is to find nearby Earth-like planets. The radial velocity (RV) and transit methods have made the main contributions to exoplanet detections. RV measurements for nearby bright stars can be made relatively efficiently and have enabled planets to be discovered around a significant fraction of them. The transit technique is relatively more sensitive to faint and distant stars. Considering the rare occurrence rate of transit events, the RV method is still of great importance for discovering nearby planets, as evidenced by the detection of Proxima Centauri b (Anglada-Escudé et al. 2016), although the *Transiting Exoplanet Survey Satellite* is poised to find thousands of nearby transit systems (e.g., Ricker et al. 2014).

Since the Earth is the only planet known to host life, a conservative path to the detection of extraterrestrial biosignatures is to find an Earth-like planet around a Sun-like star (also called an "Earth twin"). To detect such signals, we need to have high-precision RV data that is sensitive to about 0.1 m s^{-1} RV variations (Mayor et al. 2014). For less massive stars like M dwarfs, the signals corresponding to Earth-sized planets in their temperate zones (where liquid water can exist on the surface; Kopparapu et al. 2014) can be as high as 1 m s^{-1}. To distinguish from the Earth twins, we call these planets "Earth analogs." Thanks to the recent development of high-precision spectrometers, such as Echelle SPectrograph for Rocky Exoplanets and Stable Spectroscopic Observations (ESPRESSO; Pepe et al. 2010) and NN-explore Exoplanet Investigations with Doppler spectroscopy (NEID; Schwab et al. 2016), as well as advanced noise modeling and activity mitigating techniques (Feng et al. 2017b; Dumusque 2018), we are moving toward the detection sensitivity of Earth twins, though multiple issues related to stellar activity and instrumental stability (e.g., Fischer et al. 2016) still need to be resolved.

The availability of long-term, high-precision spectroscopic observations is one of the basic requirements in the discoveries of Earth analogs, such as Proxima Centauri b (Anglada-Escudé et al. 2016), GL 667 Cc (Anglada-Escudé et al. 2013), and Luyten b (Astudillo-Defru et al. 2017). To this end, the Carnegie Planet Finder Spectrograph (PFS; Crane et al. 2010) is one of the major instruments dedicated to performing a high-precision spectroscopic survey of nearby stars. Since its commissioning in 2010, it has made important contributions to the discovery (Proxima Centauri b at 1.3 pc, Anglada-Escudé et al. 2016; Barnard's star b at 1.8 pc, Ribas et al. 2018) and characterization (GJ 9827 bcd at 30 pc, Teske et al. 2018) of nearby planets.

In this work, we use PFS survey data presented in Section 2 and describe how it is processed with a signal diagnostic framework in Section 3 and apply it to the PFS survey data, and then we select signals that are statistically significant, consistent in time, uncorrelated with stellar activity indicators, and robust to the choice of noise models. We then identify planet candidates from these signals and discuss 15 of the most significant signals individually in Section 4. Finally, we conclude in Section 5.

2. Data

The PFS measures the Doppler shift of stellar spectral lines through calibration with the spectrum of iodine (e.g., Marcy & Butler 1992). The calibration and the barycentric correction of the spectrum are implemented through the procedures introduced by Butler et al. (1996). The Ca II HK (converted to the *S*-index) and the Hα lines are extracted from the spectrum to assess the stellar activity level. The photon noise is calculated through photon counts by assuming a Poisson distribution. We

* This paper includes data gathered with the 6.5 m Magellan Telescopes located at the Las Campanas Observatory, Chile.
[5] Hubble Fellow.

Table 1
Physical Parameters and Observation Parameters for PFS Targets Reported in This Paper

Star	Type	Mass ($M_\odot$)	Temperature (K)	α (deg)	δ (deg)	$\tilde{\omega}$ (mas)	Time Span (Days)	Number of RVs[a]
HD 210193	G3V	1.04 ± 0.06	5790^{+38}_{-50}	332.40	−41.23	23.67 ± 0.04	3161	26
HD 211970	K7V	0.61 ± 0.04	4127^{+149}_{-94}	335.57	−54.56	76.15 ± 0.04	3102	52
HD 39855	G8V	0.87 ± 0.05	5576^{+50}_{-46}	88.63	−19.70	42.96 ± 0.03	2271	25
HIP 35173	K2V	0.79 ± 0.05	4881^{+55}_{-81}	109.04	−3.67	30.13 ± 0.06	3269	39
HD 102843	K0V	0.95 ± 0.05	5436^{+144}_{-69}	177.59	−1.25	15.91 ± 0.05	3009	36
HD 103949	K3V	0.77 ± 0.04	4792^{+66}_{-54}	179.55	−23.92	37.71 ± 0.08	3064	48
HD 206255	G5IV/V	1.42 ± 0.08	5635^{+82}_{-99}	325.59	−50.09	13.26 ± 0.03	3099	34
HD 21411	G8V	0.89 ± 0.05	5605^{+247}_{-132}	51.55	−30.62	34.30 ± 0.04	3217	31
HD 64114	G7V	0.95 ± 0.05	5676^{+32}_{-87}	117.98	−11.03	31.69 ± 0.04	2633	28
HD 8326	K2V	0.80 ± 0.05	4914^{+51}_{-32}	20.53	−26.89	32.56 ± 0.05	3152	16
HD 164604	K3.5V	0.77 ± 0.04	4684^{+135}_{-37}	270.78	−28.56	25.38 ± 0.06	3100	19
HIP 54373	K5V	0.57 ± 0.03	4021^{+226}_{-146}	166.86	−19.29	53.40 ± 0.05	3064	51
HD 24085	G0V	1.22 ± 0.07	6034^{+32}_{-53}	56.26	−70.02	18.19 ± 0.02	3162	25
HIP 71135	M1	0.66 ± 0.04	4146^{+107}_{-110}	218.22	−52.65	30.90 ± 0.05	3009	44

Note. The astrometric parameters and the effective temperature are provided by *Gaia* DR2 (Gaia Collaboration et al. 2018). The stellar mass is derived from the *Gaia* luminosity using the mass–luminosity relationships in Malkov (2007), Eker et al. (2015), and Benedict et al. (2016). The spectral type is determined through a crossmatch of PFS targets with the Simbad database.
[a] These RVs are not binned and multiple RVs may correspond to a single epoch.

consider this photon noise to be an indicator of instrumental and/or stellar noise because it can modulate the uncertainty of RV measurements and thus change the likelihood of a periodic signal.

For all PFS targets, we find the relevant astrometry, systematic RV, and luminosity from *Gaia* data release 2 (DR2; Gaia Collaboration et al. 2018) through crossmatching using a search cone of 2′. The *Gaia* source corresponding to a PFS target is identified by selecting the brightest star among all matched sources. This approach works because most PFS targets are stars that are bright and have an apparent visual magnitude of less than 15. The mass of a star is estimated through the mass–luminosity functions introduced by Malkov (2007), Eker et al. (2015), and Benedict et al. (2016). The stellar type of each star is found by crossmatching the PFS targets with the Simbad database (Wenger et al. 2000).

3. Initial Selection of Planet Candidates

We define a signal diagnostic framework to identify signals in the PFS RV data. The following steps are used to search and constrain signals.

1. We calculate the Bayes factor periodograms (BFPs) for activity indices using Agatha (Feng et al. 2017a) and identify activity signals at periods of $P_{\rm activity}$. In the calculation of BFP, we use the first order moving average model (MA(1); Tuomi et al. 2013) to account for time-correlated noise. Compared with traditional periodograms, such as the Lomb–Scargle periodogram (Lomb 1976; Scargle 1982), the BFP is able to model the excess white noise as well as the red noise in a time series.
2. We calculate the BFPs for the RV data using the white, MA(1), and first auto-regressive (AR(1); Tuomi & Anglada-Escudé 2013) noise models and identify signals for each noise model (called "BFP signals" at periods of $P_{\rm BFP}$). Although AR(1) might lead to false negatives according to Tuomi & Anglada-Escudé (2013), we use it to test whether an RV signal is noise-model dependent.
3. We use the adaptive Markov Chain Monte Carlo (MCMC) algorithm (called "DRAM") developed by Haario et al. (2006) for model and parameter inferences. Specifically, we launch tempered (hot) chains to find the global maximum of the posterior and use nontempered (cold) chains to constrain the maximum a posterior (MAP) signal. Such a combination of hot and cold chains allows the parameter space to be well explored without getting stuck in the local maxima. This approach incorporates model complexity by considering prior distributions. Our algorithm is similar to the hybrid MCMC algorithm developed by Gregory (2011). Similar to our previous works (Feng et al. 2017b), we adopt a semi-Gaussian prior distribution with a zero mean and a 0.2 standard deviation for eccentricity to account for the eccentricity distribution found in RV planets (Kipping 2013) and in transit systems (Kane et al. 2012; Van Eylen et al. 2019). Such a broad semi-Gaussian distribution allows solutions with relatively high eccentricity but penalizes solutions with extremely high eccentricity. We adopt uniform priors for the logarithmic orbital period and for other orbital parameters.

We constrain each RV signal in the data until any additional signal does not increase the likelihood significantly. In other words, a signal is statistically significant only if its inclusion in the RV model leads to a Bayes factor (BF) of larger than 150 or $\ln(\mathrm{BF}) > 5$ (Kass & Raftery 1995; Feng et al. 2016). The BF is the ratio of marginalized likelihoods (or evidences) for two models. We derive the BF from the Bayesian information criterion following Kass & Raftery (1995). Thus, the calculation of the BF in this work assumes uniform prior distributions of model parameters. This BF criterion is found to be optimal compared with other information criteria based on analyses of simulated and real RV data sets (Feng et al. 2016). Therefore, we use the BF criterion to assess the significance of signals.

The optimal noise model is chosen according to the model comparison scheme in Agatha (Feng et al. 2017a).

Table 2
Parameters for Planet Candidates

Planet	$M_p \sin I$ ($M_\oplus$)	a (au)	P (days)	K (m s^{-1})	e	ω (deg)	M_0 (deg)
HD 210193 b	153.1 ± 23.3	1.487 ± 0.031	649.918 ± 8.599	11.40 ± 1.66	0.24 ± 0.09	168.84 ± 28.69	73.93 ± 32.63
	$167.39^{+41.04}_{-67.60}$	$1.488^{+0.071}_{-0.076}$	$650.200^{+20.030}_{-19.962}$	$12.55^{+2.70}_{-5.14}$	$0.28^{+0.16}_{-0.26}$	$171.16^{+66.34}_{-93.97}$	$75.84^{+104.08}_{-67.25}$
HD 211970 b	13.0 ± 2.5	0.143 ± 0.003	25.201 ± 0.025	4.02 ± 0.74	0.15 ± 0.10	97.83 ± 51.73	84.80 ± 48.66
	$13.28^{+5.63}_{-5.91}$	$0.143^{+0.006}_{-0.007}$	$25.193^{+0.067}_{-0.051}$	$4.04^{+1.78}_{-1.76}$	$0.07^{+0.35}_{-0.07}$	$78.83^{+125.57}_{-75.35}$	$98.86^{+89.52}_{-96.58}$
HD 39855 b	8.5 ± 1.5	0.041 ± 0.001	3.2498 ± 0.0004	4.08 ± 0.71	0.14 ± 0.11	102.97 ± 79.77	154.27 ± 77.93
	$8.89^{+3.19}_{-3.90}$	$0.041^{+0.002}_{-0.002}$	$3.2499^{+0.0007}_{-0.0010}$	$4.21^{+1.88}_{-1.76}$	$0.06^{+0.44}_{-0.06}$	$3.97^{+261.97}_{-2.44}$	$258.85^{+18.02}_{-254.96}$
HIP 35173 b	12.7 ± 2.7	0.217 ± 0.004	41.516 ± 0.077	2.80 ± 0.59	0.16 ± 0.11	10.73 ± 96.40	-7.66 ± 91.92
	$13.21^{+5.94}_{-6.69}$	$0.217^{+0.009}_{-0.010}$	$41.475^{+0.219}_{-0.137}$	$2.92^{+1.27}_{-1.51}$	$0.23^{+0.25}_{-0.22}$	$31.91^{+143.42}_{-207.31}$	$-0.89^{+175.62}_{-174.01}$
HD 102843 b	113.9 ± 14.5	4.074 ± 0.270	3090.942 ± 295.049	5.24 ± 0.61	0.11 ± 0.07	108.69 ± 49.38	104.42 ± 54.78
	$101.23^{+48.00}_{-19.99}$	$3.793^{+0.950}_{-0.315}$	$2770.962^{+1069.329}_{-312.973}$	$4.80^{+1.96}_{-0.93}$	$0.09^{+0.21}_{-0.09}$	$147.46^{+60.47}_{-141.03}$	$42.44^{+183.19}_{-37.78}$
HD 103949 b	11.2 ± 2.3	0.439 ± 0.009	120.878 ± 0.446	1.77 ± 0.35	0.19 ± 0.12	127.74 ± 68.28	234.49 ± 67.94
	$11.66^{+4.95}_{-5.69}$	$0.439^{+0.019}_{-0.021}$	$121.040^{+0.876}_{-1.199}$	$1.82^{+0.78}_{-0.89}$	$0.17^{+0.35}_{-0.17}$	$79.95^{+259.71}_{-67.49}$	$287.79^{+58.68}_{-269.95}$
HD 206255 b	34.2 ± 7.1	0.461 ± 0.009	96.045 ± 0.317	3.92 ± 0.80	0.23 ± 0.11	86.92 ± 44.90	124.46 ± 46.09
	$37.21^{+13.97}_{-19.35}$	$0.461^{+0.020}_{-0.022}$	$96.027^{+0.760}_{-0.707}$	$4.30^{+1.49}_{-2.32}$	$0.29^{+0.22}_{-0.27}$	$58.41^{+141.93}_{-50.95}$	$149.46^{+70.96}_{-133.56}$
HD 21411 b	65.9 ± 25.6	0.362 ± 0.007	84.288 ± 0.127	11.47 ± 4.33	0.40 ± 0.15	332.42 ± 17.74	285.65 ± 22.51
	$75.58^{+51.87}_{-68.06}$	$0.362^{+0.016}_{-0.017}$	$84.232^{+0.351}_{-0.239}$	$13.95^{+14.71}_{-8.55}$	$0.52^{+0.19}_{-0.46}$	$336.90^{+21.88}_{-60.98}$	$275.56^{+72.82}_{-35.60}$
HD 64114 b	17.8 ± 3.5	0.246 ± 0.005	45.791 ± 0.070	3.33 ± 0.64	0.12 ± 0.08	215.30 ± 85.53	209.15 ± 85.31
	$17.97^{+8.01}_{-8.33}$	$0.246^{+0.011}_{-0.012}$	$45.799^{+0.156}_{-0.172}$	$3.33^{+1.52}_{-1.57}$	$0.00^{+0.38}_{-0.00}$	$107.07^{+249.84}_{-89.00}$	$342.18^{+14.14}_{-323.83}$
HD 8326 b	66.6 ± 19.6	0.533 ± 0.011	158.991 ± 1.440	9.36 ± 2.72	0.20 ± 0.11	-44.79 ± 36.46	272.91 ± 39.43
	$74.20^{+38.76}_{-52.97}$	$0.535^{+0.023}_{-0.027}$	$159.662^{+2.719}_{-3.970}$	$10.35^{+6.55}_{-6.71}$	$0.20^{+0.31}_{-0.19}$	$-35.07^{+35.00}_{-111.79}$	$276.95^{+75.77}_{-113.13}$
HD 164604 b	635.0 ± 82.3	1.331 ± 0.029	641.472 ± 10.129	60.66 ± 6.97	0.35 ± 0.10	65.40 ± 15.11	40.01 ± 25.82
	$663.82^{+168.84}_{-213.66}$	$1.323^{+0.075}_{-0.061}$	$635.218^{+30.166}_{-16.782}$	$65.04^{+12.46}_{-21.11}$	$0.42^{+0.17}_{-0.33}$	$65.35^{+35.80}_{-39.81}$	$29.06^{+115.92}_{-26.12}$
HIP 54373 b	8.62 ± 1.84	0.063 ± 0.001	7.760 ± 0.003	4.19 ± 0.87	0.20 ± 0.11	72.34 ± 44.58	90.73 ± 43.89
	$8.80^{+4.18}_{-4.37}$	$0.063^{+0.003}_{-0.003}$	$7.760^{+0.006}_{-0.007}$	$4.17^{+2.25}_{-1.96}$	$0.10^{+0.41}_{-0.09}$	$65.31^{+115.57}_{-63.27}$	$103.03^{+84.33}_{-96.47}$
HIP 54373 c	12.44 ± 2.11	0.099 ± 0.002	15.144 ± 0.008	4.84 ± 0.79	0.20 ± 0.12	122.37 ± 60.04	242.71 ± 57.33
	$12.87^{+4.60}_{-5.25}$	$0.099^{+0.004}_{-0.005}$	$15.145^{+0.019}_{-0.020}$	$5.00^{+1.73}_{-2.04}$	$0.24^{+0.26}_{-0.23}$	$91.65^{+236.96}_{-69.59}$	$268.06^{+70.26}_{-232.15}$
HD 24085 b	11.8 ± 3.1	0.034 ± 0.001	2.0455 ± 0.0002	5.40 ± 1.37	0.22 ± 0.12	8.92 ± 54.83	156.74 ± 60.90
	$14.40^{+4.66}_{-9.56}$	$0.034^{+0.001}_{-0.002}$	$2.0455^{+0.0005}_{-0.0004}$	$6.68^{+2.40}_{-4.36}$	$0.31^{+0.20}_{-0.30}$	$7.86^{+146.67}_{-166.98}$	$149.95^{+180.97}_{-132.94}$
HIP 71135 b	18.8 ± 4.1	0.335 ± 0.007	87.190 ± 0.381	3.71 ± 0.79	0.21 ± 0.13	115.60 ± 71.72	223.03 ± 73.08
	$19.51^{+9.07}_{-10.04}$	$0.335^{+0.015}_{-0.016}$	$87.186^{+0.884}_{-0.875}$	$3.79^{+1.87}_{-1.94}$	$0.19^{+0.38}_{-0.18}$	$82.29^{+250.40}_{-76.63}$	$253.41^{+87.17}_{-243.15}$

Note. The minimum mass, semimajor axis, period, RV semi-amplitude, eccentricity, and mean anomaly at the reference epoch are denoted by $M_p \sin I$, a, P, K, e, ω, and M_0, respectively. The mean and standard deviation of each parameter are estimated from the posterior samples drawn by MCMC. For each parameter, the value at the MAP and the uncertainty interval defined by the 1% and 99% quantiles of the posterior distribution are shown below the values of the mean and standard deviation. The orbit of HD 164604 b is significantly eccentric because $e = 0$ is more than 3σ away from the mean. The orbital eccentricities for all other planet candidates are consistent with zero.

According to the comparison of various noise models for both synthetic and real RV data sets (Feng et al. 2016), the MA models are optimal for avoiding false positives and negatives. Hence, we compare the lower and higher order MA models by calculating their BFs. We select the most complex model (with the highest order) that passes the criterion of $\ln(\mathrm{BF}) > 5$. For example, we calculate the maximum likelihoods for the white noise, MA(1), MA(2), and MA(3) models for an RV data set. The logarithmic BFs for MA(1) and the white noise model and for MA(2) and MA(1) are larger than five, while the logarithmic BF for MA(3) and MA(2) is less than five. The optimal noise model would be MA(2) because it is complex enough to model the time-correlated noise in the data and is simple enough to avoid overfitting.

4. We define a moving time window and calculate the BFP for each step. In other words, we calculate BF(P_i, W_j) (or BF_{ij}) for the ith period for the jth time window (W_j) and form a two-dimensional power spectrum. Because the number of RVs in different time windows is different, we normalize BF_{ij} for each time window to compare the consistency of signals across time windows. Specifically, we scale the maximum BF for time window W_j to one through $\mathrm{BF}'_j = \mathrm{BF}_j / \max(\mathrm{BF}_j)$, where $\mathrm{BF} = \{\mathrm{BF}_{1j}, \mathrm{BF}_{2j}, \mathrm{BF}_{3j}, \ldots\}$. To optimize the visualization of the significance of signals as a function of time, the window sizes and steps are chosen according to the sampling and size of the data, as well as the period of target signal. For example, for a set of 100 RVs sampled uniformly over a time span of one year, we can divide the time span into 12 bins and calculate the BFP for the RVs in each bin or time window to investigate the time consistency of signals with orbital periods less than 30 days. For long-period signals, broader time windows should be defined. This example provides a rule of thumb for the choice of window sizes and steps. We call this two-dimensional BFP the "moving periodogram." It is used to check the time consistency of signals identified by MCMC (called "MCMC signals" at periods of P_{MCMC}). We refer the readers to Feng et al. (2017a) for more details.

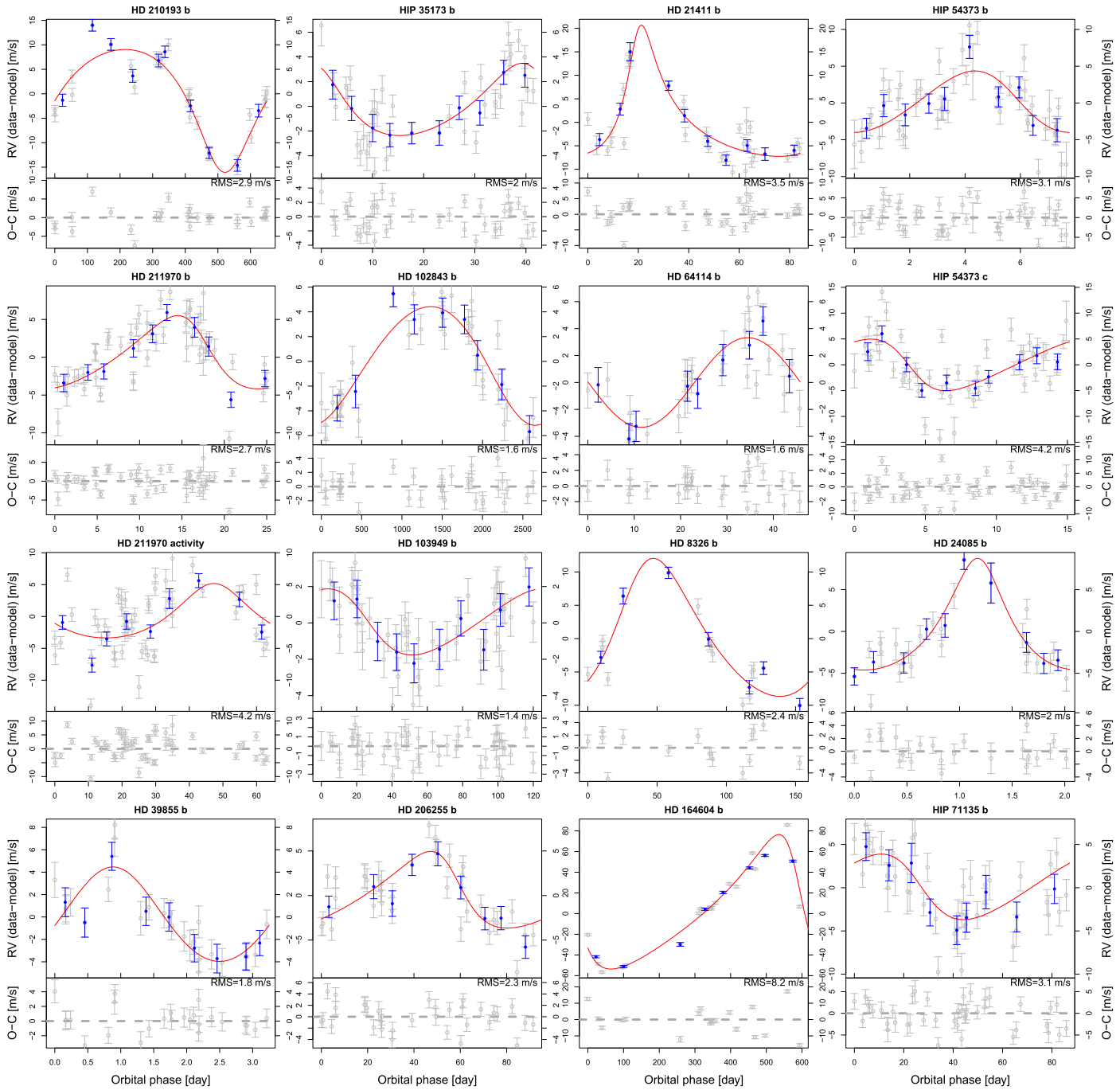

Figure 1. Phase curve and corresponding residuals for all planet candidates. The blue error bars show the error-weighted average RVs in 10 bins. The best orbital solution is determined by the MAP values of orbital parameters. The rms of the residual RVs is shown in each panel.

5. We assess the overall quality of an MCMC signal. A genuine Keplerian (due to a planet) signal should:
   (a) be robust in the choice of noise models. The difference between the period of the MCMC signal and the corresponding BFP signals is less than 10% (i.e., $0.9\,P_{\rm BFP} < P_{\rm MCMC} < 1.1\,P_{\rm BFP}$).
   (b) not be caused by stellar activity. The difference between the period of the MCMC signal and the signals with the two highest BFs for each activity index is less than 10% (i.e., $P_{\rm MCMC} < 0.9\,P_{\rm activity}$ or $P_{\rm MCMC} > 1.1\,P_{\rm activity}$).
   (c) be statistically significant. The MCMC signal passes the ln(BF) threshold of 5.
   (d) be consistent in time. For an MCMC signal at a period of $_{Pi}$, the standard deviation of $\mathrm{BF}'_i = \{\mathrm{BF}'_{i1}, \mathrm{BF}'_{i2}, \mathrm{BF}'_{i3}, \ldots\}$ should be less than 0.5.

The above criteria are aimed at selecting as many candidate signals as possible and at removing obvious false positives. Hence, the signals identified through these criteria will be further studied to investigate their origin. To examine the overlap between two signals, we adopt a 20% period window centered at the period of one of the two signals. This use of a period ratio or percentage rather than a constant period is consistent with our use of the uniform distribution as the prior of the logarithmic period. This period window is narrow for long-period signals that are

Table 3
PFS Data for the 14 Targets

Star	BJD(TDB) (days)	RV ($m\ s^{-1}$)	RV Error ($m\ s^{-1}$)	*S*-index	Hα	Photon Count
HD 210193	2455255.7322	−2.96	1.03	0.2681	0.03949	17240
HD 210193	2455427.74325	10.5	1.19	0.1453	0.0298	20808
HD 210193	2455853.59631	−3.87	1.2	0.1457	0.03015	29319
HD 210193	2456139.71964	6.04	1.26	0.1408	0.03059	34033
HD 210193	2456150.73734	1.68	1.34	0.1459	0.03024	17527
HD 210193	2456507.78955	−8.57	1.22	0.1407	0.03049	33751
HD 210193	2456551.68262	−0.75	1.8	0.1522	−1	23658
HD 210193	2456556.69412	−3.99	1.44	0.1589	0.031	16623
HD 210193	2456867.80008	7.54	1.35	0.153	0.02991	29091
HD 210193	2456883.72837	7.57	1.15	0.1475	0.03002	41296
HD 210193	2457198.88933	−1.32	1.2	0.1479	0.02977	33208
HD 210193	2457205.83287	0.43	1.3	0.1532	0.02989	40291
HD 210193	2457258.62318	3.76	1.32	0.1588	0.03054	27175
HD 210193	2457259.74463	0	1.32	0.1558	0.03054	21843
HD 210193	2457321.59187	14.24	1.2	0.1562	0.02954	24402
HD 210193	2457529.88662	6.59	1.25	0.1457	0.0302	23762
HD 210193	2457554.90868	10.2	1.21	0.1586	0.03064	21573
HD 210193	2457614.76154	−1.31	1.13	0.1468	0.03049	36335
HD 210193	2457620.6494	0.09	1.32	0.1514	−1	20191
HD 210193	2458266.85745	−0.13	1.11	−1	−1	16288
HD 210193	2458270.89806	−4.68	1.14	−1	−1	22104
HD 210193	2458293.82287	−5.82	1.3	−1	−1	18573
HD 210193	2458329.77738	−11.74	1.08	−1	−1	7636
HD 210193	2458329.78116	−12.28	1.24	−1	−1	7132
HD 210193	2458416.55692	−15.24	1.17	−1	−1	7138
HD 210193	2458416.5608	−13.7	1.22	−1	−1	7617
HD 211970	2455255.7322	−2.96	1.03	0.2681	0.03949	17240
HD 211970	2455427.75376	4.39	1.01	1.0036	0.05437	24542
HD 211970	2455439.7522	4.22	1.16	0.9017	0.05306	20281
HD 211970	2455785.66778	−6.38	1.17	0.6735	0.05198	22935
HD 211970	2455787.78384	−5.22	1.11	0.7317	0.05236	25121
HD 211970	2455790.64196	−0.3	1.15	0.7294	0.05265	20023
HD 211970	2455793.66157	−5.06	1.2	0.8489	0.05269	17699
HD 211970	2455795.73434	2	1.11	0.724	0.05198	21689
HD 211970	2455801.6949	2.91	1.24	0.8221	0.05361	12861
HD 211970	2455802.66507	3.1	1.26	0.7252	0.05326	14089
HD 211970	2455843.73573	0.23	1.26	0.4834	0.05189	15628
HD 211970	2455844.62917	−1.09	1.05	0.6433	0.05282	17331
HD 211970	2455845.65818	−3.1	1.07	0.6588	0.05241	16444
HD 211970	2455846.6955	−1.07	1.1	0.6576	0.05249	21090
HD 211970	2455850.66816	3.63	1.2	0.6687	0.0551	13526
HD 211970	2455851.6625	1.67	1.27	0.5961	0.05486	14869
HD 211970	2455852.63469	−0.86	1.29	0.6993	0.05403	13643
HD 211970	2455853.60615	−1.63	1.43	0.5476	0.05468	10524
HD 211970	2456085.91961	−4.78	1.14	0.7777	0.05213	20813
HD 211970	2456086.82561	−3.88	1.02	0.8023	0.05236	25862
HD 211970	2456087.91929	−5.73	1.45	0.9308	0.05402	10622
HD 211970	2456092.87766	0.67	1.07	0.874	0.0524	23615
HD 211970	2456141.7073	0.99	1.12	0.8227	0.05365	23515
HD 211970	2456147.73551	5.39	1.57	0.8008	−1	9014
HD 211970	2456501.7777	6.74	1.24	0.8439	0.05292	18659
HD 211970	2456504.84093	1.5	1.86	0.9769	0.05405	6983
HD 211970	2456504.84951	6	1.71	0.9942	0.05364	7662
HD 211970	2456506.79608	0.47	1.86	0.9598	0.05385	6825
HD 211970	2456506.80612	9.49	3.55	0.9492	0.05433	3374
HD 211970	2456555.60902	3.43	1.15	0.729	0.05246	19106
HD 211970	2456556.72102	−2.35	1.17	0.8122	0.05351	15289
HD 211970	2456603.58858	6.93	1.03	0.576	0.05298	24254
HD 211970	2456610.55366	−13.6	1.03	0.5361	0.05267	22999
HD 211970	2456816.93005	−10.69	1.79	0.881	0.0543	7642
HD 211970	2456818.87738	−4.42	1.08	0.7789	0.05211	25940
HD 211970	2456866.72527	−5.89	1.05	0.7527	0.05193	27615
HD 211970	2456871.73924	−2.41	1.13	0.7926	0.05235	16594

Table 3
(Continued)

Star	BJD(TDB) (days)	RV ($m\ s^{-1}$)	RV Error ($m\ s^{-1}$)	*S*-index	Hα	Photon Count
HD 211970	2456876.83292	2.96	1.24	0.8458	0.05245	19119
HD 211970	2456879.717	0.6	1.08	0.8207	0.05307	26605
HD 211970	2457198.89566	−1.7	1.08	0.8817	0.05225	20889
HD 211970	2457203.81436	2.47	1.15	0.9188	0.0538	23365
HD 211970	2457260.7319	0	1.18	0.7327	0.05214	17234
HD 211970	2457321.5985	−5.3	1.07	0.4997	0.05319	19970
HD 211970	2457536.92111	8.42	1.24	0.9646	0.05503	15202
HD 211970	2457555.8774	−2.5	1.05	0.8753	0.05301	24541
HD 211970	2457614.77018	4.04	1.14	0.9375	0.05419	26397
HD 211970	2457621.70646	−0.82	1.05	0.8482	0.05353	20522
HD 211970	2458293.84928	4.73	1.07	−1	−1	8166
HD 211970	2458329.78811	−3.74	0.96	−1	−1	7189
HD 211970	2458355.67643	−5.71	0.87	−1	−1	6828
HD 211970	2458357.60275	−5.85	1.04	−1	−1	4154
HD 211970	2458357.60651	−5.93	0.85	−1	−1	4515
HD 39855	2455255.7322	−2.96	1.03	0.2681	0.03949	17240
HD 39855	2455200.69318	3.74	1.57	0.2162	−1	17422
HD 39855	2455255.58202	−3.12	1.13	0.1975	0.03123	32336
HD 39855	2455587.59977	1.07	1.26	0.1736	0.03222	20347
HD 39855	2455587.60343	1.21	1.21	0.1694	0.033	20166
HD 39855	2455669.49598	2.9	1.09	0.1835	0.03233	46028
HD 39855	2455845.83806	0.78	1.31	0.1667	0.03186	21890
HD 39855	2455852.86337	0	1.42	0.1635	0.03258	19112
HD 39855	2455956.63819	−1.3	1.31	0.159	0.03182	36101
HD 39855	2456281.72155	−2.11	1.37	0.1665	−1	23915
HD 39855	2456284.67998	0.75	1.19	0.1669	0.03205	49974
HD 39855	2456345.5798	8.65	1.22	0.0324	0	24537
HD 39855	2456356.60133	−4.48	1.17	0.166	0.03208	31425
HD 39855	2456358.57618	7.48	1.65	0.2344	0.03372	9358
HD 39855	2456695.62685	−0.22	1.28	0.1807	0.03197	36301
HD 39855	2456703.59108	1.3	1.13	0.1992	0.03261	31290
HD 39855	2457029.69333	−3.62	1.25	0.1645	0.03183	53474
HD 39855	2457053.61031	−0.06	1.3	0.1691	0.0319	40647
HD 39855	2457123.51006	−1.78	1.1	0.1692	0.03184	33114
HD 39855	2457267.88973	1.74	1.23	0.1609	0.03221	36153
HD 39855	2457325.81241	−3.09	1.27	0.1599	0.03185	43264
HD 39855	2457389.6711	−0.3	1.31	0.1606	0.03181	45327
HD 39855	2457395.70227	0.32	1.5	0.1663	0.03228	17590
HD 39855	2457448.5851	−3.36	1.11	0.1677	0.03151	53217
HD 39855	2457471.52459	−2.9	1.31	0.1635	0.03179	30674
HIP 35173	2455255.7322	−2.96	1.03	0.2681	0.03949	17240
HIP 35173	2455200.71753	6.59	1.68	0.3799	−1	7620
HIP 35173	2455252.62714	−5.32	1.19	0.2378	−1	18749
HIP 35173	2455581.64495	−3.75	1.05	0.2705	0.04027	23076
HIP 35173	2455956.68819	−3.17	1.02	0.2119	0.03946	24086
HIP 35173	2455957.64998	−0.34	1.69	0.3684	0.04145	5933
HIP 35173	2456284.73876	2.24	0.99	0.2187	0.03928	25479
HIP 35173	2456291.77672	−4.32	0.91	0.2199	0.03931	21960
HIP 35173	2456343.62157	−2.2	0.99	0.2358	0.03954	21343
HIP 35173	2456354.57027	0.3	0.99	0.2249	0.03952	18295
HIP 35173	2456357.61684	4.18	0.94	0.2159	0.03952	19493
HIP 35173	2456610.82296	1.19	1.01	0.2045	0.03912	21836
HIP 35173	2456692.67294	1.23	1	0.2117	0.03897	25266
HIP 35173	2456696.62238	−0.12	1.06	0.2266	0.03968	19352
HIP 35173	2456698.67353	1.45	0.85	0.2184	0.03961	22937
HIP 35173	2456729.6363	3.45	0.96	0.1861	0.03963	25493
HIP 35173	2456730.59016	3.84	1.04	0.2392	0.03957	19102
HIP 35173	2456733.59673	3.92	0.93	0.2016	0.03951	23207
HIP 35173	2457020.72449	5.8	0.93	0.2355	0.03905	25335
HIP 35173	2457022.71547	5.23	0.88	0.2298	0.03988	26572
HIP 35173	2457030.75951	0.67	0.99	0.2397	0.04002	23900
HIP 35173	2457050.6369	−0.88	0.93	0.2361	0.03982	25437

Table 3
(Continued)

Star	BJD(TDB) (days)	RV ($m\ s^{-1}$)	RV Error ($m\ s^{-1}$)	*S*-index	Hα	Photon Count
HIP 35173	2457053.622	−2.14	1.05	0.2335	0.04009	16408
HIP 35173	2457060.6255	0.71	0.99	0.2171	0.03874	21750
HIP 35173	2457069.61469	1.56	1.07	0.2294	0.03968	16376
HIP 35173	2457118.54054	−0.58	0.93	0.2351	0.03967	26280
HIP 35173	2457122.53949	−0.06	0.89	0.2355	0.03954	23231
HIP 35173	2457324.87053	−3.88	1.42	0.3246	0.04145	9338
HIP 35173	2457327.85226	1.26	1.13	0.2742	0.04025	14149
HIP 35173	2457387.66829	−3.02	0.88	0.2645	0.04026	24824
HIP 35173	2457396.65701	−0.68	1.04	0.2645	0.03957	19286
HIP 35173	2457448.62086	−2.62	1.05	0.2613	0.04009	25338
HIP 35173	2457471.54655	2.21	1.07	0.2645	0.04011	15211
HIP 35173	2457499.53549	−2.28	0.87	0.2483	0.03952	30511
HIP 35173	2457737.74108	−3.26	1.08	0.2444	0.039	26502
HIP 35173	2457758.74084	1.8	0.9	0.2517	0.04008	22330
HIP 35173	2457762.65955	0	1.07	0.2701	0.03987	23516
HIP 35173	2457824.59241	−0.76	0.99	0.2622	0.03915	18743
HIP 35173	2458469.83192	−0.13	1	−1	−1	4885
HD 102843	2455255.7322	−2.96	1.03	0.2681	0.03949	17240
HD 102843	2455200.83576	0	2.43	0.2557	−1	5708
HD 102843	2455252.79165	−1.84	1.26	0.1589	−1	14798
HD 102843	2455342.58244	−0.1	1.26	0.1976	0.03497	14379
HD 102843	2455585.824	2.86	1.31	0.1616	0.03431	15311
HD 102843	2455664.67782	−1.93	1.32	0.21	0.0337	15991
HD 102843	2456093.53284	7.9	1.06	0.3384	0.03394	13810
HD 102843	2456288.8541	4.36	1.15	0.1613	0.0343	19078
HD 102843	2456345.79961	7.62	1.18	0.1877	0.03412	17302
HD 102843	2456435.55492	4.65	1.22	0.1722	0.03345	19933
HD 102843	2456694.81016	7.42	1.13	0.1816	0.03405	20088
HD 102843	2456698.78069	5.44	1.17	0.1787	0.03419	18673
HD 102843	2456701.73522	5.79	1.21	0.173	0.03419	17658
HD 102843	2456730.72343	3.96	1.22	0.1926	0.03423	15830
HD 102843	2456817.53906	6.99	1.37	0.2421	0.03412	14105
HD 102843	2457023.84581	4.55	1.1	0.1748	0.03459	17749
HD 102843	2457029.83073	3.92	1.08	0.1635	0.0334	20407
HD 102843	2457065.81831	6.29	1.25	0.1613	0.03409	14638
HD 102843	2457069.72688	4.24	1.22	0.1656	0.03448	14364
HD 102843	2457119.70904	0.6	1.22	0.1677	0.03355	17706
HD 102843	2457203.49054	−0.26	1.17	0.158	0.03388	18199
HD 102843	2457206.51837	−0.76	1.1	0.1546	0.03372	20241
HD 102843	2457390.84293	3.21	1.14	0.1521	0.03421	17726
HD 102843	2457397.84159	−1.19	1.22	0.1608	0.03427	12809
HD 102843	2457448.79186	−0.79	1.23	0.1565	0.03404	22385
HD 102843	2457472.68105	−4.12	1.3	0.1531	0.03406	19522
HD 102843	2457505.60482	−2.59	1.29	0.1656	0.03407	15096
HD 102843	2457760.85002	−5.58	1.14	0.1479	0.0342	21243
HD 102843	2457829.80843	−3.93	1.6	0.2068	0.0341	11045
HD 102843	2458204.66791	−3.35	0.93	−1	−1	14073
HD 102843	2458204.71316	−4.14	1	−1	−1	13154
HD 102843	2458205.72943	−3.62	1.03	−1	−1	13330
HD 102843	2458206.68341	−3.11	1.05	−1	−1	12668
HD 102843	2458207.70655	−2.38	0.98	−1	−1	14300
HD 102843	2458208.63571	−2.28	0.94	−1	−1	19760
HD 102843	2458209.65381	−3.39	0.93	−1	−1	20254
HD 103949	2455255.7322	−2.96	1.03	0.2681	0.03949	17240
HD 103949	2455200.85365	1.87	1.57	0.2838	−1	7861
HD 103949	2455252.80669	−4.49	1.19	0.2311	−1	18529
HD 103949	2455342.59972	1.02	1.05	0.1979	0.04018	29944
HD 103949	2455584.81107	1.87	1.03	0.2294	0.04103	23085
HD 103949	2455664.70212	−1.29	1.1	0.2303	0.04016	24463
HD 103949	2456093.54236	−0.55	0.99	0.2439	0.04117	16120
HD 103949	2456284.85339	3.57	1	0.2749	0.0407	24711
HD 103949	2456345.81626	−3.56	1.03	0.2768	0.0409	26003

Table 3
(Continued)

Star	BJD(TDB) (days)	RV ($m\ s^{-1}$)	RV Error ($m\ s^{-1}$)	*S*-index	Hα	Photon Count
HD 103949	2456356.81978	−2.33	1.12	0.2896	0.04172	20181
HD 103949	2456431.59876	−0.01	1.59	0.2572	0.04084	21637
HD 103949	2456434.58574	−1.51	1.05	0.2804	0.04086	21799
HD 103949	2456438.57712	0.27	1.13	0.2702	0.04101	19845
HD 103949	2456501.4829	−2.1	1.24	0.2944	0.04111	14991
HD 103949	2456693.77863	−4.52	0.98	0.2627	0.04093	33792
HD 103949	2456696.74631	−2.93	1.04	0.2767	0.0402	22235
HD 103949	2456700.78295	0.22	0.96	0.2344	0.04033	23764
HD 103949	2456702.70173	−0.47	1.05	0.2669	0.04105	22201
HD 103949	2456729.7549	−1.08	0.94	0.2666	0.03986	41798
HD 103949	2456730.73207	0.41	1.02	0.2827	0.04008	24473
HD 103949	2456816.56657	−1.35	1.28	0.2531	0.04054	23830
HD 103949	2457022.81444	2.14	0.9	0.2581	0.04022	25317
HD 103949	2457026.8595	−0.68	0.96	0.2575	0.04001	19568
HD 103949	2457051.86844	−1.99	1	0.2518	0.0401	24487
HD 103949	2457064.70854	−1.16	1.03	0.2449	0.04014	21884
HD 103949	2457118.69169	−2.56	1.05	0.2416	0.04088	26524
HD 103949	2457123.69519	0.34	1.05	0.2494	0.0411	21538
HD 103949	2457200.48178	−1	1.09	0.2458	0.04072	23451
HD 103949	2457389.80697	0.96	1.04	0.2319	0.04031	18497
HD 103949	2457396.86666	2.12	0.97	0.2184	0.04079	21717
HD 103949	2457450.78222	−0.99	1.1	0.2338	0.03996	23609
HD 103949	2457472.71043	−1	1.04	0.2142	0.04002	23336
HD 103949	2457478.70621	−0.58	0.99	0.2063	0.03953	37022
HD 103949	2457505.62043	2.32	1.06	0.2133	0.03972	23868
HD 103949	2457555.52785	−0.85	1.13	0.2765	0.04002	22711
HD 103949	2457760.859	1.99	0.92	0.2064	0.04058	36733
HD 103949	2457761.81112	3.34	0.91	0.2053	−1	36580
HD 103949	2457765.79163	0	1.08	0.2084	0.04087	21426
HD 103949	2457825.75799	1.52	0.95	0.2212	0.04043	26191
HD 103949	2457862.66605	0.07	1.11	0.2366	0.03969	16008
HD 103949	2458203.69321	1.08	0.87	−1	−1	21612
HD 103949	2458204.75568	2.05	0.88	−1	−1	15853
HD 103949	2458205.74082	2.23	0.88	−1	−1	22214
HD 103949	2458206.67226	1.42	0.83	−1	−1	19816
HD 103949	2458207.71827	1.48	0.81	−1	−1	21013
HD 103949	2458208.62537	0.8	0.83	−1	−1	22948
HD 103949	2458209.64388	0.82	0.79	−1	−1	20962
HD 103949	2458264.57394	−0.63	0.91	−1	−1	19389
HD 206255	2455255.7322	−2.96	1.03	0.2681	0.03949	17240
HD 206255	2455427.71742	−2.66	1.3	0.1349	0.02973	21832
HD 206255	2455439.73885	−4.03	1.32	0.1355	0.03028	18934
HD 206255	2455796.7401	2.49	1.4	0.1427	0.03018	19100
HD 206255	2455850.65044	2.32	1.26	0.1429	0.02996	19692
HD 206255	2455850.65416	2.34	1.4	0.1444	0.02997	19669
HD 206255	2456086.81919	−1.77	1.18	0.1315	0.02905	39826
HD 206255	2456092.85872	−1.16	1.23	0.1297	0.03006	25348
HD 206255	2456139.70543	1.73	1.27	0.1338	0.02995	23160
HD 206255	2456144.7747	2.14	1.65	0.1404	0.03056	13672
HD 206255	2456150.7277	−0.11	1.44	0.131	0.02972	18626
HD 206255	2456504.83089	−3.38	1.32	0.1362	0.03007	20147
HD 206255	2456506.78512	1.91	1.32	0.142	0.02958	20609
HD 206255	2456550.62471	7.66	1.43	0.3088	0.02968	32231
HD 206255	2456553.6186	4.55	1.47	0.1388	0.02961	21158
HD 206255	2456604.54902	−4.1	1.23	0.1347	0.02951	26861
HD 206255	2456817.86837	0.09	1.23	0.1319	0.02993	31069
HD 206255	2456866.69534	−3.18	1.31	0.1284	0.02972	39119
HD 206255	2456876.68366	−9.05	1.29	0.1275	0.02919	39943
HD 206255	2457198.86731	−1.8	1.34	0.1267	0.02996	27749
HD 206255	2457206.83583	−2.37	1.43	0.1242	0.02971	38134
HD 206255	2457258.61859	−2.48	1.31	0.1298	0.02977	30047
HD 206255	2457321.57596	5.79	1.37	0.1304	0.0296	26552
HD 206255	2457327.61917	3.74	1.3	0.129	0.02982	24059

Table 3
(Continued)

Star	BJD(TDB) (days)	RV ($m\ s^{-1}$)	RV Error ($m\ s^{-1}$)	*S*-index	Hα	Photon Count
HD 206255	2457536.90929	−5.04	1.31	0.1341	0.0296	23177
HD 206255	2457555.86064	−5.31	1.21	0.1229	0.02888	43387
HD 206255	2457614.71064	0	1.2	0.1293	0.02955	38830
HD 206255	2457620.63101	−4.69	1.37	0.1404	−1	20427
HD 206255	2458271.77631	2.13	1.19	−1	−1	17530
HD 206255	2458293.81535	1.92	1.21	−1	−1	20410
HD 206255	2458334.76763	−1.66	1.18	−1	−1	6918
HD 206255	2458334.77142	0.67	1.21	−1	−1	7649
HD 206255	2458354.67918	−2.19	1.44	−1	−1	4487
HD 206255	2458354.68676	0	1.41	−1	−1	4517
HD 21411	2455255.7322	−2.96	1.03	0.2681	0.03949	17240
HD 21411	2455200.62078	5.04	1.34	0.2286	−1	13359
HD 21411	2455430.89198	−0.25	1.36	0.2078	0.03409	20044
HD 21411	2455584.57744	2.11	1.18	0.2027	0.03301	21664
HD 21411	2455852.79817	−6.04	1.46	0.1842	0.03321	19016
HD 21411	2456143.9235	19.35	1.93	0.1895	−1	12955
HD 21411	2456281.63855	−2.43	1.33	0.2106	−1	25027
HD 21411	2456290.59309	−3.22	0.92	0.1861	0.03291	39304
HD 21411	2456343.53765	−1.08	1.04	0.1941	0.03295	24919
HD 21411	2456358.52243	4.55	2.91	0.3238	0.03612	3820
HD 21411	2456551.8202	−0.56	1.97	0.2034	−1	23523
HD 21411	2456605.70767	−6.31	1.41	0.2024	0.03334	22103
HD 21411	2456612.67223	3.34	1.25	0.1946	0.03323	30911
HD 21411	2456697.5676	−4.21	1.04	0.1869	0.03265	32159
HD 21411	2456866.90825	−2.66	1.32	0.1951	0.03274	26895
HD 21411	2456882.92219	−1.71	1.34	0.1947	0.03284	36006
HD 21411	2457022.63789	−3.14	1.01	0.196	0.03318	36914
HD 21411	2457029.63113	3	0.96	0.1996	0.0331	30569
HD 21411	2457053.52375	−1.31	1.2	0.1995	0.03282	21376
HD 21411	2457061.56943	−1.68	1.05	0.1944	0.03258	23471
HD 21411	2457260.8869	1.71	1.46	0.1854	0.03264	21551
HD 21411	2457320.75509	−0.14	1.28	0.1889	0.0329	22339
HD 21411	2457389.61809	0	0.98	0.1808	0.03256	35380
HD 21411	2457622.92626	−0.93	1.29	0.1882	0.03299	25644
HD 21411	2457741.62792	11.4	1.28	0.2188	0.03356	37117
HD 21411	2457759.59214	12.12	0.98	0.4113	0.03345	26847
HD 21411	2457765.62903	8.83	1.27	0.2267	0.03378	18377
HD 21411	2458410.70071	0.12	1.15	−1	−1	6032
HD 21411	2458410.70461	2.18	1.15	−1	−1	5966
HD 21411	2458417.74652	17.64	1.39	−1	−1	3519
HD 21411	2458417.75021	17.21	1.36	−1	−1	4550
HD 64114	2455255.7322	−2.96	1.03	0.2681	0.03949	17240
HD 64114	2455200.75154	−0.15	1.31	0.2264	−1	13346
HD 64114	2455255.63455	−1.84	1.31	0.2038	0.03093	39062
HD 64114	2455586.77045	−2.2	1.24	0.1658	0.03165	20608
HD 64114	2455588.6773	−0.93	1.05	0.1662	0.03134	32884
HD 64114	2455671.55327	−3.56	1.12	0.2606	0.03134	45495
HD 64114	2456288.7264	6.35	1.06	0.1931	0.03201	41494
HD 64114	2456290.78816	6.76	1.02	0.1901	0.03203	46531
HD 64114	2456345.63885	−1.92	1.34	0.0318	0	27065
HD 64114	2456695.68081	2.47	1.22	0.1977	0.03172	24676
HD 64114	2456702.66536	−0.27	1.03	0.174	0.03123	42052
HD 64114	2456733.60378	0.43	1.09	0.1725	0.0309	37678
HD 64114	2456734.61888	0.66	1.03	0.1925	0.03118	41885
HD 64114	2457021.71572	4.38	1	0.1766	0.03171	37198
HD 64114	2457024.75524	4.53	1.05	0.1732	0.03228	42179
HD 64114	2457053.66366	−1.5	1.38	0.179	0.03179	23599
HD 64114	2457061.63104	0.62	1.12	0.1723	0.03153	23509
HD 64114	2457066.61776	3.57	1.29	0.1754	0.03175	19556
HD 64114	2457117.56268	1.4	1.12	0.257	0.03123	43344
HD 64114	2457122.55954	1.09	1.14	0.1829	0.0312	43004
HD 64114	2457387.7083	0.06	0.89	0.1676	−1	44362

Table 3
(Continued)

Star	BJD(TDB) (days)	RV ($m\ s^{-1}$)	RV Error ($m\ s^{-1}$)	*S*-index	Hα	Photon Count
HD 64114	2457395.66312	−1.26	1.32	0.1695	0.03179	20384
HD 64114	2457468.59249	−1.25	1.09	0.1994	0.03131	44770
HD 64114	2457499.55607	−4.62	1.13	0.1788	0.03112	45070
HD 64114	2457740.73137	0	1.2	0.1793	0.0316	34668
HD 64114	2457761.70022	1.89	1.18	0.1765	−1	36217
HD 64114	2457769.75899	−0.32	1.26	0.1745	0.03163	25866
HD 64114	2457833.59771	−0.31	1.02	0.2028	0.03161	25333
HD 8326	2455255.7322	−2.96	1.03	0.2681	0.03949	17240
HD 8326	2455585.54494	1.02	0.93	0.2795	0.03895	23077
HD 8326	2456141.9085	1.63	0.93	0.2996	0.03954	21201
HD 8326	2456173.80187	−2.34	1.18	0.3144	0.03946	19470
HD 8326	2456612.6198	7.2	1.15	0.2793	0.03956	20615
HD 8326	2456866.87142	−3.69	0.97	0.3533	0.03979	24202
HD 8326	2456877.86915	8.75	1.19	0.3872	0.03964	21502
HD 8326	2457022.60447	2.08	0.78	0.3289	0.03911	24195
HD 8326	2457261.87244	0	1.14	0.3374	0.04018	18113
HD 8326	2457324.71174	−7.66	1.05	0.2769	0.03915	21787
HD 8326	2457389.55141	12.24	0.85	0.3446	0.03958	22770
HD 8326	2457617.86045	−2.06	0.95	0.2911	0.03929	22645
HD 8326	2457739.57509	1.28	0.91	0.2429	0.03867	24241
HD 8326	2457762.5492	−7.57	1.01	0.2622	0.0384	18459
HD 8326	2457767.5642	−6.47	0.94	0.2491	0.03803	23125
HD 8326	2458407.70844	−2.62	0.97	−1	−1	7325
HIP 31609	2455255.7322	−2.96	1.03	0.2681	0.03949	17240
HIP 31609	2458407.8526	−10.6	1.38	−1	−1	1890
HIP 31609	2458408.85256	0.43	1.44	−1	−1	2290
HIP 31609	2458409.84653	−0.03	1.61	−1	−1	1786
HIP 31609	2458410.84883	5.98	1.39	−1	−1	1854
HIP 31609	2458411.85426	6.32	1.21	−1	−1	2563
HIP 31609	2458412.85539	7.35	1.37	−1	−1	2603
HIP 31609	2458414.85554	6.52	1.68	−1	−1	1516
HIP 31609	2458415.80466	0.65	1.52	−1	−1	2027
HIP 31609	2458416.84913	−5.34	1.36	−1	−1	2229
HIP 31609	2458417.78781	−4.53	1.8	−1	−1	1330
HIP 31609	2458418.84782	3.99	1.37	−1	−1	2197
HIP 31609	2458467.77358	−6.71	1.19	−1	−1	2795
HIP 31609	2458467.8106	−4.61	1.51	−1	−1	2272
HIP 31609	2458468.75877	−9.98	1.27	−1	−1	2637
HIP 31609	2458468.81937	−12.14	1.21	−1	−1	2516
HIP 31609	2458469.76285	−7.79	1.35	−1	−1	1833
HIP 31609	2458469.82074	−10.52	1.54	−1	−1	1670
HIP 31609	2458471.76184	−7.42	1.41	−1	−1	2250
HIP 31609	2458471.83237	−12.98	1.43	−1	−1	1684
HIP 31609	2458473.76748	−5.48	1.13	−1	−1	2773
HIP 31609	2458473.83554	0	1.34	−1	−1	1845
HIP 31609	2458474.71356	0.35	1.26	−1	−1	2174
HIP 31609	2458474.82237	0.53	1.57	−1	−1	1908
HIP 31609	2458475.73745	6.98	1.38	−1	−1	2239
HIP 31609	2458475.83545	10.06	1.28	−1	−1	2198
HIP 31609	2458476.76185	11.97	1.45	−1	−1	2264
HIP 31609	2458476.84509	9.29	1.28	−1	−1	2364
HIP 54373	2455255.7322	−2.96	1.03	0.2681	0.03949	17240
HIP 54373	2455200.81388	−0.01	3.3	1.1365	−1	3251
HIP 54373	2455254.65524	−5.75	1.38	1.2993	−1	9665
HIP 54373	2455341.55657	−1	1.44	1.0644	0.06204	8371
HIP 54373	2455582.82444	−1.95	1.35	1.4122	0.0628	8352
HIP 54373	2455668.64626	3.41	1.53	1.1943	0.06075	6572
HIP 54373	2455672.54785	11.35	1.81	1.1771	0.0637	5709
HIP 54373	2455954.79749	3.3	1.45	1.5138	0.06136	7566
HIP 54373	2455955.79678	4.54	1.53	1.4293	0.06109	6743
HIP 54373	2455957.82077	9.43	3.81	1.3056	0.06466	2210

Table 3
(Continued)

Star	BJD(TDB) (days)	RV ($m\ s^{-1}$)	RV Error ($m\ s^{-1}$)	*S*-index	Hα	Photon Count
HIP 54373	2455958.80249	4.63	1.7	1.4975	0.06263	5216
HIP 54373	2455959.80289	3.33	1.51	1.5661	0.06282	6459
HIP 54373	2455960.80708	−0.08	1.57	1.4675	0.06325	5887
HIP 54373	2456086.51118	−0.64	1.48	0.9156	0.05982	8747
HIP 54373	2456088.528	3.92	1.79	0.876	0.06047	5976
HIP 54373	2456092.50926	2.43	2.68	1.0897	0.06162	3342
HIP 54373	2456093.49839	0.85	1.5	0.8899	0.06177	4120
HIP 54373	2456282.84604	−5.35	1.51	1.4307	0.06256	7443
HIP 54373	2456288.83793	−1.11	1.3	1.5356	0.06108	7256
HIP 54373	2456292.84185	7.97	1.32	1.4246	0.06095	7182
HIP 54373	2456344.72208	−3.99	1.68	1.4487	0.06154	6179
HIP 54373	2456353.74857	14.91	1.58	1.0695	0.06313	6197
HIP 54373	2456356.78344	−11.1	1.66	1.4895	0.06219	5956
HIP 54373	2456428.55774	8.18	1.86	1.0544	0.06211	5817
HIP 54373	2456433.55267	−13.61	1.77	1.0966	0.0624	6182
HIP 54373	2456434.5606	−12.48	3.04	1.1327	0.06307	2929
HIP 54373	2456438.56787	7.56	2.2	1.0119	0.06025	4376
HIP 54373	2456693.75493	−4.85	1.33	1.4456	0.06084	8806
HIP 54373	2456696.73138	3.04	1.41	1.5517	0.06225	7912
HIP 54373	2456698.75589	−2.94	1.43	1.4152	0.06235	7353
HIP 54373	2456701.71882	4.8	1.51	1.4904	0.06203	6851
HIP 54373	2456734.73037	−0.39	1.36	1.3109	0.06347	8708
HIP 54373	2456735.71095	−1.82	1.42	1.421	0.06248	6898
HIP 54373	2456818.49057	4.89	1.67	0.8612	0.0608	5877
HIP 54373	2457021.84001	1.8	1.15	1.6562	0.06457	10807
HIP 54373	2457026.82576	−0.99	1.28	1.6873	0.06407	11485
HIP 54373	2457051.75433	6.1	1.32	1.6401	0.06481	8960
HIP 54373	2457062.72414	0	1.48	1.4429	0.0605	7730
HIP 54373	2457120.68354	0	1.43	1.2376	0.06137	9716
HIP 54373	2457203.47387	−1.62	1.5	1.1355	0.06207	6658
HIP 54373	2457387.8144	−4.92	1.26	1.7353	0.06515	8091
HIP 54373	2457397.80848	0.66	1.5	1.7506	0.06575	6829
HIP 54373	2457448.74521	−1.84	1.5	1.5171	0.06162	8295
HIP 54373	2457473.66083	1.81	1.52	1.4173	0.06234	8871
HIP 54373	2457478.66936	5.97	1.3	1.2089	0.06035	9693
HIP 54373	2457499.6386	−3.47	1.49	1.0454	0.06117	9651
HIP 54373	2457559.48686	−0.38	1.26	1.0418	0.06163	11132
HIP 54373	2457759.83236	4.75	1.32	1.4273	0.06249	10217
HIP 54373	2457824.71916	−2.79	1.74	1.4785	0.06239	7142
HIP 54373	2457848.57423	2.37	1.43	1.4862	0.0641	9027
HIP 54373	2458264.55224	−5	1.08	−1	−1	6014
HD 24085	2455255.7322	−2.96	1.03	0.2681	0.03949	17240
HD 24085	2455582.60234	−1.46	1.08	0.1352	0.02901	23031
HD 24085	2455582.60495	5.07	1.2	0.1546	0.02952	15946
HD 24085	2456145.91788	0.84	1.9	0.1528	0.0293	16842
HD 24085	2456290.6024	0	1.09	0.1333	0.02865	44667
HD 24085	2456551.82884	8.13	2.39	0.1996	−1	23351
HD 24085	2456606.70671	6.58	1.52	0.1481	−1	18894
HD 24085	2456698.55207	3.42	1.24	0.1376	0.02833	31582
HD 24085	2456871.92807	−0.14	1.72	0.1322	0.0281	34132
HD 24085	2457022.6474	−0.19	1.11	0.1333	0.02843	46090
HD 24085	2457029.63619	−1.5	1.01	0.4486	0.02856	34399
HD 24085	2457053.53884	−1.5	1.2	0.1425	0.02804	21504
HD 24085	2457066.53534	−1.9	1.32	0.1423	0.02915	18847
HD 24085	2457262.87843	−0.19	1.31	0.1383	0.02889	25690
HD 24085	2457319.79348	−6.56	1.31	0.1408	0.02874	23074
HD 24085	2457389.61345	−2.7	1.07	0.1307	0.0284	40886
HD 24085	2457450.51648	−3.32	1.54	0.2745	0.02785	36913
HD 24085	2457621.92363	1.77	1.46	0.1484	0.02901	19681
HD 24085	2457741.63286	1.73	1.24	0.1384	0.02812	39691
HD 24085	2457761.60444	0.11	0.99	0.1469	−1	36598
HD 24085	2457766.5965	10.82	1.15	0.1383	0.02767	31505
HD 24085	2458354.90321	0.8	1.44	−1	−1	5261

Table 3
(Continued)

Star	BJD(TDB) (days)	RV ($m\ s^{-1}$)	RV Error ($m\ s^{-1}$)	*S*-index	Hα	Photon Count
HD 24085	2458410.70939	2.52	1.36	−1	−1	6274
HD 24085	2458410.71321	0.55	1.36	−1	−1	5865
HD 24085	2458417.75784	−1.6	1.22	−1	−1	9685
HIP 71135	2455255.7322	−2.96	1.03	0.2681	0.03949	17240
HIP 71135	2455342.66134	−0.84	1.81	0.6097	0.05082	6564
HIP 71135	2455423.50522	2.75	1.56	0.4679	0.05022	6871
HIP 71135	2455437.47257	5.23	1.44	0.4713	0.04998	7527
HIP 71135	2455785.52424	5.55	1.71	0.6408	0.05044	5343
HIP 71135	2455787.50123	4.29	1.58	0.5024	0.05042	6782
HIP 71135	2455793.49665	0	2.74	0.9498	0.05275	3198
HIP 71135	2455796.52697	1.33	2.21	0.6912	0.05062	3804
HIP 71135	2455801.50064	−0.41	2.6	0.6665	0.05317	3256
HIP 71135	2455802.48336	−1.87	2.52	0.8015	0.05235	3236
HIP 71135	2455802.49089	2.99	4.08	0.6045	0.05228	2347
HIP 71135	2455803.49751	5.78	2.06	0.6305	0.05074	4124
HIP 71135	2455804.51336	6.2	2.46	0.8024	0.05122	3173
HIP 71135	2455958.86941	7.28	1.7	0.4351	0.04957	5545
HIP 71135	2456085.68322	0.21	1.99	0.5965	0.05015	5509
HIP 71135	2456094.5975	0.37	2.22	0.6373	0.05039	4013
HIP 71135	2456344.81656	−6.35	1.6	0.6323	0.04945	7260
HIP 71135	2456347.86443	−4.46	1.47	0.5509	0.04972	6454
HIP 71135	2456352.84684	−3.15	1.56	0.4161	0.04915	7537
HIP 71135	2456355.82826	−1.64	1.62	0.473	0.04994	5795
HIP 71135	2456357.83352	0.88	2.26	0.7276	0.05083	3488
HIP 71135	2456433.68066	−9.55	1.96	0.5104	0.0495	5171
HIP 71135	2456435.64872	−3.37	1.79	0.502	0.04961	7090
HIP 71135	2456505.53671	−1.55	1.89	0.5166	0.05004	5215
HIP 71135	2456505.54627	−2.26	1.8	0.5029	0.05041	4960
HIP 71135	2456693.83985	−3.02	1.65	0.6546	0.04985	7995
HIP 71135	2456696.85337	−4.25	1.66	0.4446	0.04991	7582
HIP 71135	2456698.88682	1.17	2.02	0.5201	0.05064	4152
HIP 71135	2456729.81559	−1.66	1.47	0.4786	0.04997	7362
HIP 71135	2456733.82888	3.99	1.76	0.4666	0.04992	6573
HIP 71135	2456734.82708	−2.76	1.64	0.5633	0.05004	6805
HIP 71135	2456817.66181	−3.13	2.28	0.7852	0.05095	4477
HIP 71135	2457067.85988	1.33	1.67	0.482	0.04926	6457
HIP 71135	2457120.74646	−3.59	1.71	0.5834	0.04968	8725
HIP 71135	2457204.58631	2.37	1.65	0.4521	0.05029	7820
HIP 71135	2457265.48913	1.58	1.5	0.5086	0.05034	7955
HIP 71135	2457449.88976	1.41	1.51	0.4015	0.04978	11195
HIP 71135	2457500.82204	−6.79	1.69	0.5521	0.04979	8611
HIP 71135	2457534.66035	4.6	1.92	0.7042	0.05033	5762
HIP 71135	2457557.60976	−9.73	1.77	0.452	0.04921	8042
HIP 71135	2457626.49196	4	1.52	0.5047	0.04976	7897
HIP 71135	2457825.8283	−5.28	1.76	0.5633	0.04923	8850
HIP 71135	2457850.80439	−4.94	1.82	0.4754	0.05018	6916
HIP 71135	2458264.68979	−3.07	1.46	−1	−1	4145

Note. The nonvalid values in the tables are denoted by −1.

typically not well constrained but is broad for short-period ones that are well constrained by the data. Because most of our data sets have a short time span and cannot be used to identify long-period signals (e.g., a few years), the period window is broad enough to exclude most false short-period signals, although it might also exclude real long-period signals. On the other hand, RV signals might be the harmonics of activity signals that are outside of the period window and, thus, cannot be rejected through this criterion. However, such a scenario is unlikely because we use two signals in each activity index to identify overlaps, and the harmonics are unlikely to pass all other criteria if it is due to activity.

Although we use a moving periodogram to check the consistency of signals in time, it may not always show consistent power, even if a signal is genuine, because the power in the BFP for a given time window is also determined by the time span of the window, the sampling of the data, and the period of the signal. For example, if the period of a signal is longer than the time span of the whole data set, there would be no time window that can cover one period and, thus, a moving periodogram is not suitable for a consistency test. In this case, our algorithm would still count the signal satisfying the time-consistency criterion, although further analyses are needed to investigate the nature of such signals.

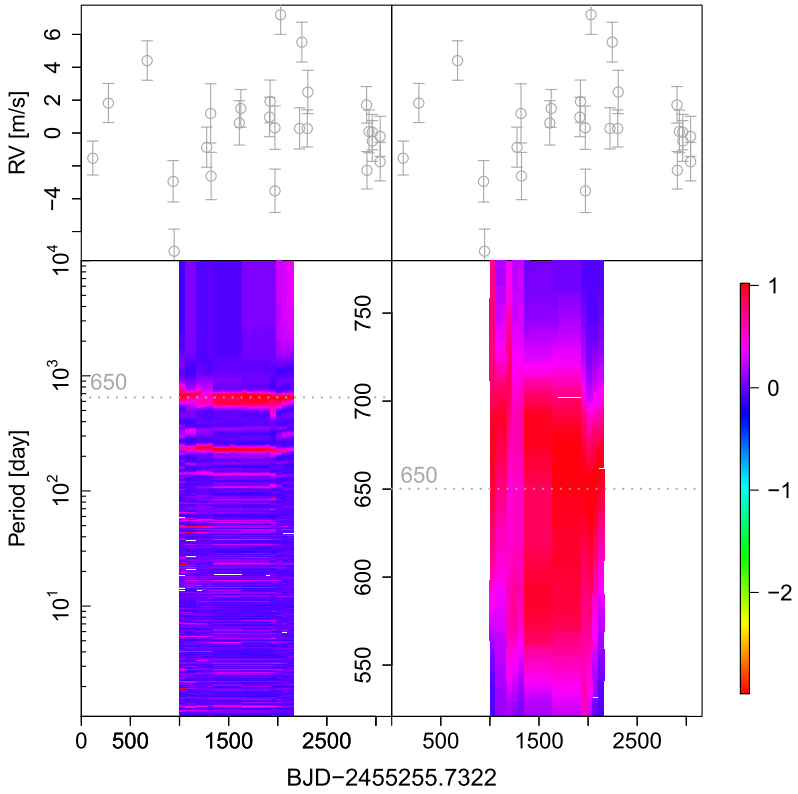

Figure 2. Moving periodogram for the PFS data for HD 210193. The top panels show RV data. The bottom right panel is a zoomed-in version of the bottom left panel, which shows the color-coded two-dimensional BFP. The x-axis is the BJD time relative to the first epoch. The periodogram power is normalized for each moving time window so that the BF does not depend on the number of RVs in each window. A global color coding is applied to these normalized BFs. The time span of each time window is 2036 days. The window move to cover the full data set within 20 steps. In the calculation of BFPs, we ignore the eccentricity of signals. This is not likely to change the time consistency of MCMC signals, although such assumption may alternate signal period and amplitude slightly.

Since many of our PFS data sets contain less than 50 RVs, we are cautious about whether a signal can be reliably detected and whether the instrument is stable enough for the detection of long-period signals. We use two criteria to deal with these problems. First, we use the moving periodogram to check the consistency of signals to diagnose the stability of spectrograph and to check the time consistency of signals. Second, we avoid overfitting by comparing the null hypothesis and the planet hypothesis in the Bayesian framework. We use $\ln(\mathrm{BF}) > 5$ (Kass & Raftery 1995; Raftery 1995) to select the best model. Since the null hypothesis is typically favored by BF (Kass & Raftery 1995), we expect few false positives in our automated signal identification. A similar conclusion has been drawn by Feng et al. (2016) based on a comparison of various information criteria in the analyses of simulated and real RV data sets. Considering that most short-period Keplerian orbits are not eccentric (Kipping 2013), there are typically less than five efficient free parameters for a Keplerian orbit, although we calculate the BF using five parameters to penalize complex models. Hence, the BF criterion is conservative enough to avoid overfitting.

The application of the diagnostic procedure to 534 PFS data sets leads to an identification of 480 periodic signals. We assign the quality flag of "A" to a signal if it satisfies all of the four criteria, "B" if it fails to pass one criterion, "C" if it fails to pass two criteria, "D" if it only passes one criterion, and "E" if it satisfies no criterion. By the automated analyses, we find 42, 173, 192, 67, and 5 signals with quality "A," "B," "C," "D," and "E," respectively. We further investigate the "A" and "B" quality signals and select 15 planetary candidates to report. These targets do not have available data from other instruments and, thus, are suitable for our automated algorithm, which is aimed at identifying signals in RVs measured by a single instrument. We will design an updated algorithm for automated analyses of data sets from multiple instruments in upcoming work. The physical and observational properties for the stars in these systems are shown in Table 1.

4. Results

The parameters of planet candidates are inferred from the posterior samples drawn by DRAM chains and are shown in Table 2. The phase curves of all planet candidates and activity signals are shown in Figure 1. In the calculation of BFPs for noise models, we do not use the Gaussian process (GP) as many previous studies did (Haywood et al. 2014; Rajpaul et al. 2015) because the GP could lead to false negatives, according to recent studies (Dumusque 2016; Feng et al. 2016; Ribas et al. 2018). Moreover, an appropriate kernel for activity modeling is typically not known if the rotation period and activity life span are not well determined. We perform a uniform analysis of PFS targets in this work and could explore incorporating GPs informed by photometric data available in the future. Hence, we cannot determine the rotation periods of most stars except in the cases that rotation-induced activity signals can be found both in activity indices and in RVs.

The RV signal corresponding to a candidate is typically consistently found in different data chunks, as shown in the moving periodogram (e.g., see Figure 2 for HD 210193). As mentioned in Section 3, the moving periodogram may not be

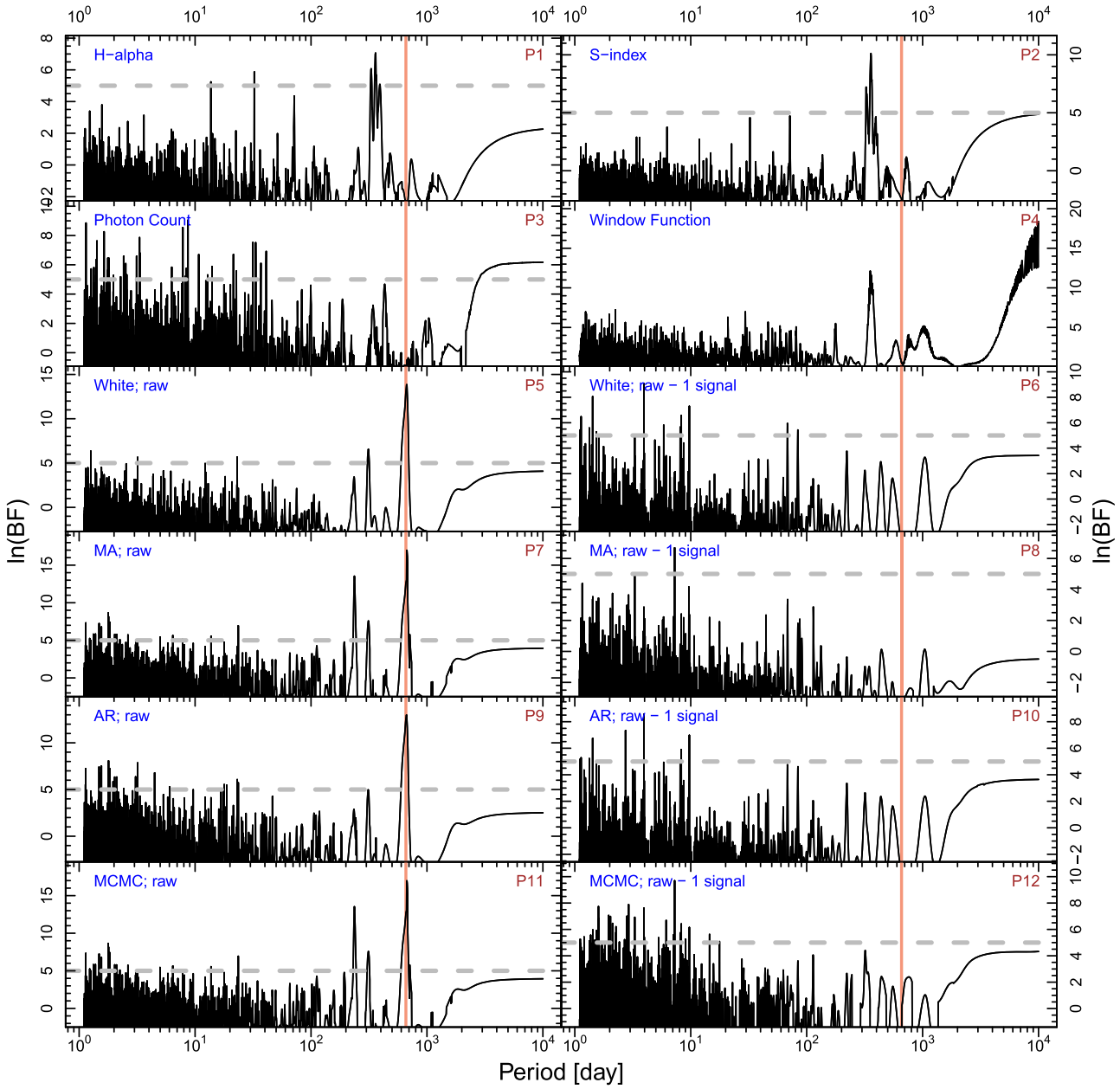

Figure 3. BFPs for HD 210193. The BFPs are calculated for the activity indices and for the white noise model, MA(1), and AR(1) for the raw RV data and RVs with sinusoidal signals subtracted. The BFPs for activity indices are calculated using the MA(1) model. The window function is calculated using the Lomb–Scargle periodogram (Lomb 1976; Scargle 1982). The activity indices, window function, noise models, and data sets are shown in the top left corners. Each panel is denoted by "Px" in the top right corner where "x" is a natural number. The RV signal at a period of 650 days is marked by the red vertical lines. The panels denoted by "MCMC" show the BFPs for the raw data subtracted by the best-fit Keplerian signals constrained by MCMC. The gray dashed line denotes the ln(BF) = 5 criterion in each BFP. The elements in this figure are also applicable for the subsequent figures. The signals in the residual BFPs are either noise-model dependent or not identified as significant signals through MCMC sampling.

suitable for all signals, thus, we only show them for the RV signals that need further confirmation. We also calculate the BFPs for activity indices and do not find any overlap between activity signals and the Keplerian signals. We display these in a series of plots from Figure 3 onward where subplots P1 are for Hα etc. The 14 PFS data sets are shown in Table 3.

We discuss the results for individual cases as follows.

1. *HD 210193* is a G star with a mass of 1.04 $M_{\odot}$ and a distance of 42.25 pc. The planet candidate has a minimum mass of 153 $M_{\oplus}$ and an orbital period of about 650 days. It is a warm giant planet located in the temperate zone with the inner and outer boundaries corresponding to orbital periods of 256 and 926 days, respectively, according to Kopparapu et al. (2014).

We also calculate the BFPs for activity indices and do not find any overlap between activity signals and the Keplerian signal, as shown in Figure 3. The phase curve in Figure 1 shows a good fit of the one-planet model to the RV data in terms of phase coverage and high statistical significance (i.e., ln(BF) = 10.9). The corresponding RV signal is consistently found in different data chunks, as shown in the moving periodogram (see Figure 2).

There are also other short-period signals shown in the BFPs for residual RVs (P6, P8, P10, and P12 in Figure 3),

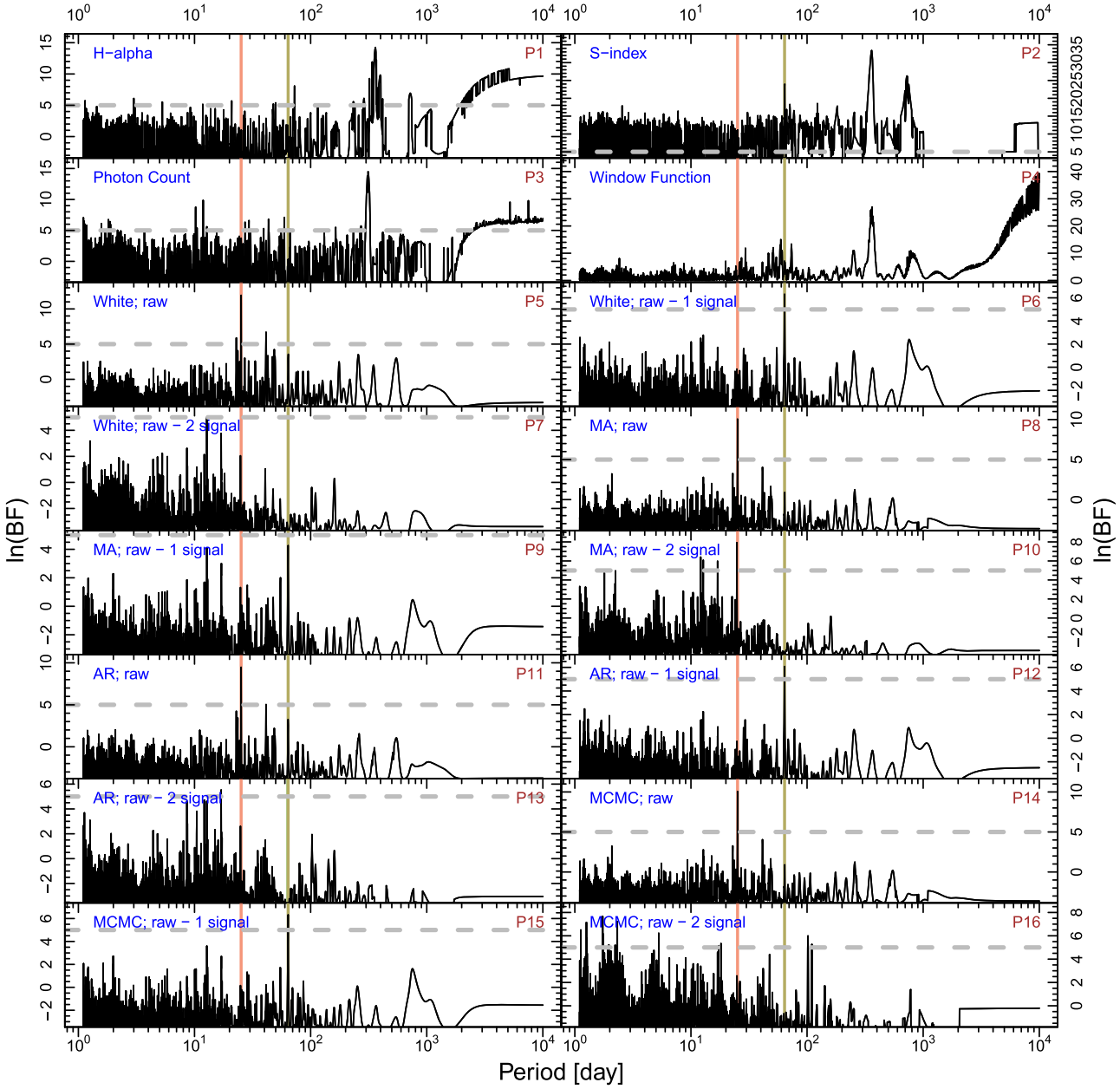

Figure 4. BFPs for HD 211970. The red line shows the Keplerian signal at a period of 25.2 days, while the green line shows the 64.0-day activity signal.

but they are either not significant or depend on the choice of noise models.

2. *HD 211970* (GJ 1267) is a K star with a mass of 0.61 $M_{\odot}$. It is about 13 pc away from the Sun and is the nearest star in this reported sample. The planet candidate is consistent with a Neptune with a minimum mass of 13.92 $M_{\oplus}$ and an orbital period of 25.2 days.

   We also identify an activity signal at a period of 64.0 days. This activity signal shows strong power in the BFPs for RVs and the *S*-index (Figure 4). A Keplerian fit of the activity signal to the RV data shows nonzero eccentricity and large residuals with a rms of 4.2 m s^{-1} (see Figure 1), suggesting an origin caused by the quasi-periodic differential rotation of the star that cannot be properly modeled by deterministic periodic functions. Thus, the rotation period of this star is probably 64 days. Because the true model of activity signal is not known, we report the orbital parameters for the planet candidate based on the MCMC posterior sampling for a one-planet model.
3. *HD 39855* is a G star with a mass of 0.87 $M_{\odot}$ and a distance of 23.28 pc. The planet candidate is consistent with a hot super-Earth with a minimum mass of 8.5 $M_{\oplus}$ and an orbital period of 3.25 days. The corresponding RV signal is not evident in the BFPs for the *S*-index and Hα shown in Figure 5.
4. *HIP 35173* is a K star with a mass of 0.79 $M_{\odot}$ and a distance of 33.19 pc. The planet candidate is consistent with a Neptune with a minimum mass of 12.7 $M_{\oplus}$ and an orbital period of 41.5 days. The corresponding RV signal is not evident in the BFPs for the activity indices of the *S*-index and Hα shown in Figure 6. This signal is also consistently strong in various data chunks, as seen from the moving periodogram in Figure 7.

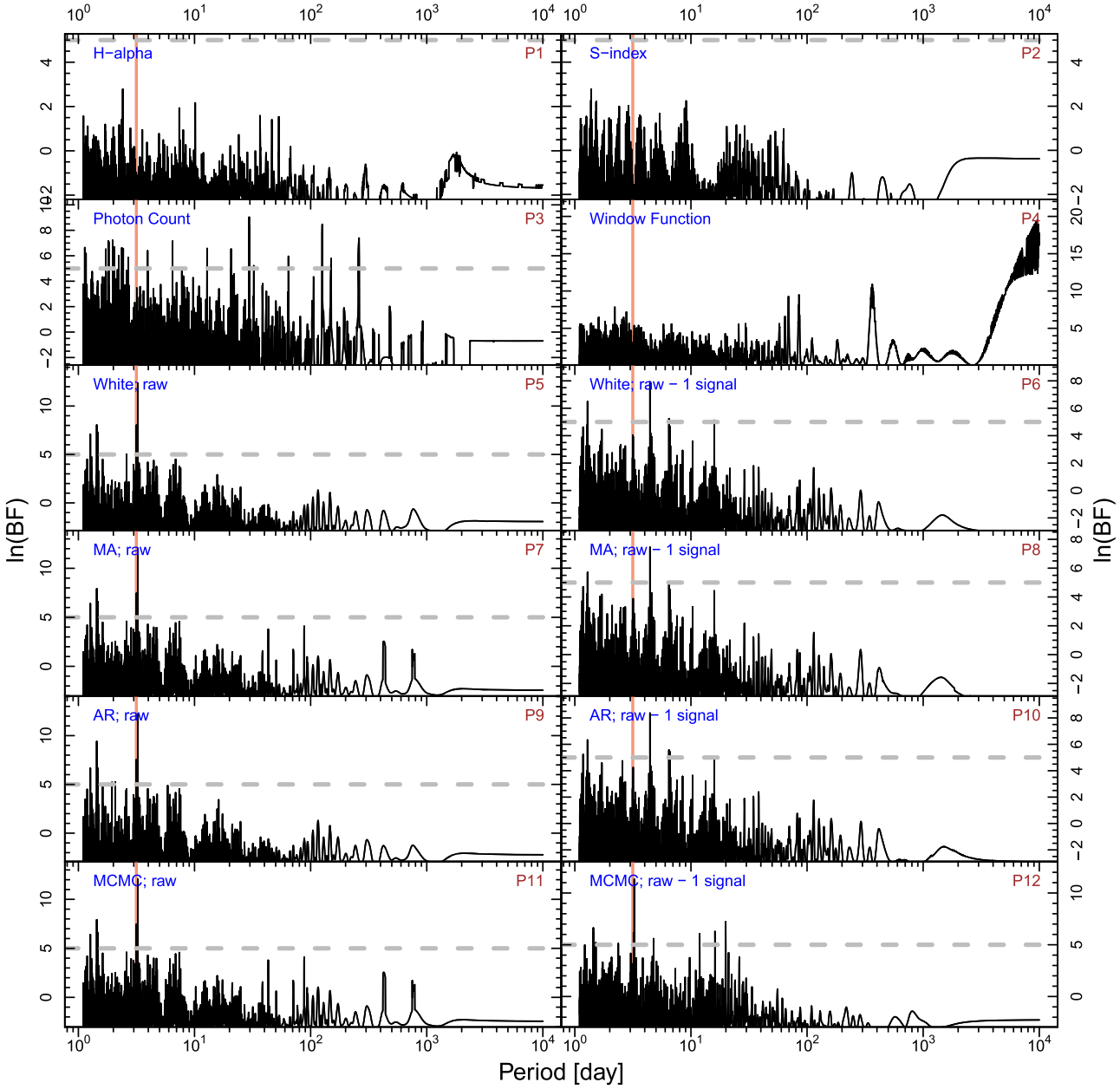

Figure 5. BFPs for HD 39855. The red line shows the signal at a period of 3.25 days.

5. *HD 102843* is a K star with a mass of 0.95 $M_{\odot}$ and a distance of 62.87 pc. The planet candidate is consistent with a cool Saturn with a minimum mass of 114 $M_{\oplus}$ and an orbital period of 3090 days. Due to its long orbital period, the time span of the data is not long enough to cover multiple orbital periods and, thus, the moving periodogram is not appropriate for a test of time consistency. This signal is statistically significant (ln(BF) = 7.7; also see Figure 1) and is unique in the BFPs for various noise models (see Figure 8). On the other hand, the BFP for Hα shows a signal with a period much longer than the RV signal, probably arising from the magnetic cycle.
6. *HD 103949* is a K star with a mass of 0.77 $M_{\odot}$ and a distance of 26.52 pc. The planet candidate has a minimum mass of 11.2 $M_{\oplus}$ and an orbital period of 121 days. It is a warm Neptune located in the temperate zone. The corresponding RV signal is not evident in the BFPs for the activity indices of the *S*-index and Hα shown in Figure 9.
7. *HD 206255* is a G star with a mass of 1.42 $M_{\odot}$ and a distance of 75.40 pc. The planet candidate is consistent with a Neptune with a minimum mass of 34.2 $M_{\oplus}$ and an orbital period of 96.0 days.

The corresponding RV signal is unique and has an eccentricity consistent with zero, as indicated by the posterior distribution. Thus, the extra number of free parameters of the one-planet model with respect to the zero-planet model is better when set to three instead of five in the calculation of BF. The former leads to ln(BF) = 8.1, while the latter to ln(BF) = 4.6. Although the latter does not pass the ln(BF) > 5 criterion, we count it as a valid planet candidate due to the above considerations in the calculation of ln(BF) and also because it satisfies all other criteria (see Figure 10).

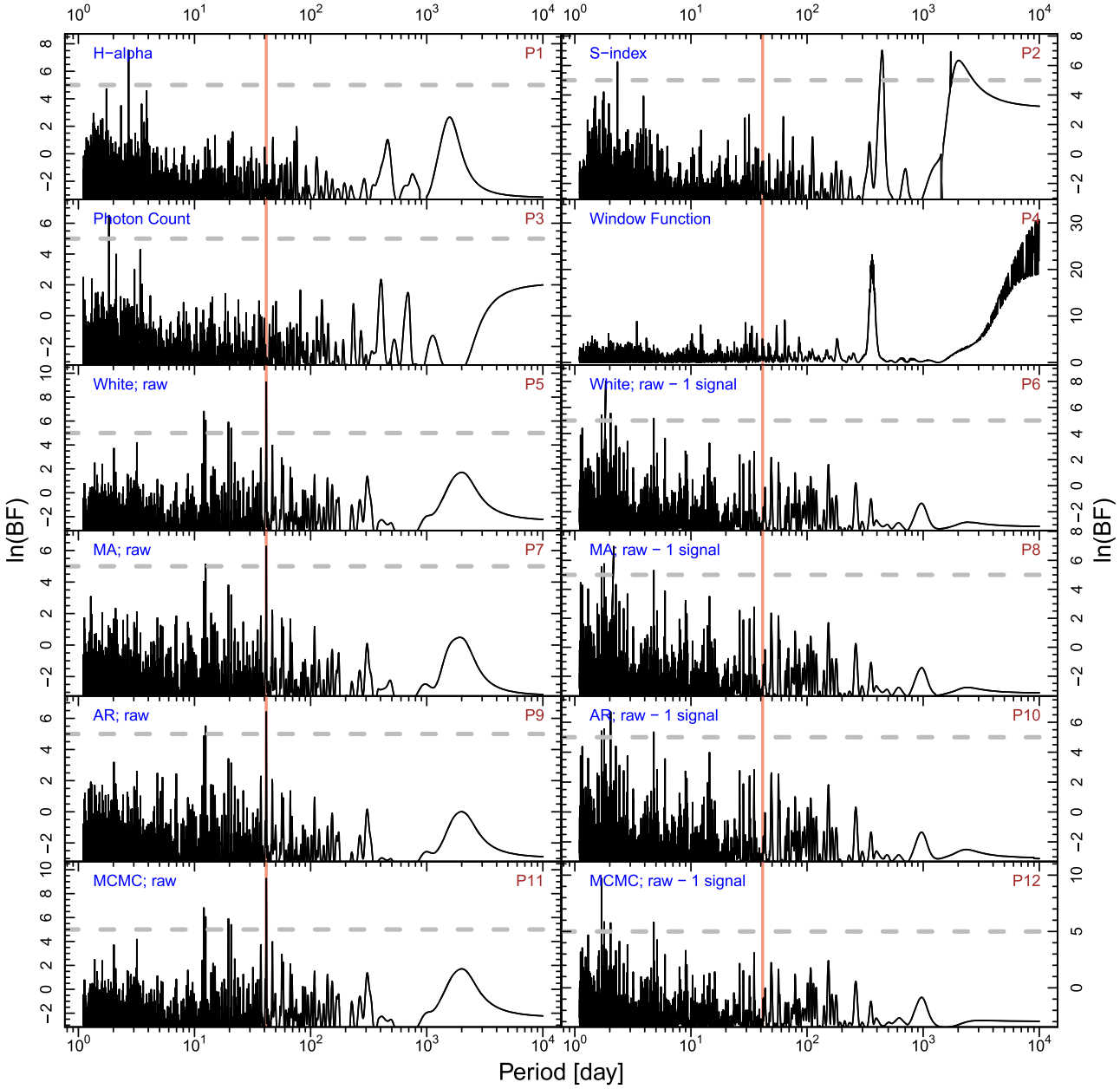

Figure 6. BFPs for HIP 35173. The red line shows the signal at a period of 41.5 days.

8. *HD 21411* is a G star with a mass of 0.89 $M_{\odot}$ and a distance of 29.16 pc. The planet candidate is consistent with a Neptune with a minimum mass of 65.8 $M_{\oplus}$ and an orbital period of 84.3 days.

   However, the corresponding signal is not as strong as the 18.8 days signal in the BFP (see Figure 11), probably due to its high eccentricity ($e = 0.4$) and the assumption of circular orbit in the calculation of BFP. To confirm the signal, we launch multiple MCMC chains and find the same significant 18.8 days signal, leading to ln(BF) = 13.2. We also constrain the 84.3 and 18.8 days signals simultaneously and find that the two-planet model has a logarithmic BF of 2.8 with respect to the one-planet model. Thus, we conclude that the 84.3 days signal is significant, while the 18.8 days signal is not significant enough to report. The 18.8 days signal is not see in the BFPs for the *S*-index and Hα; further follow-up observations are needed to investigate the nature of this signal.
9. *HD 64114* is a G star with a mass of 0.95 $M_{\odot}$ and a distance of 31.55 pc. The planet candidate is consistent with a Neptune with a minimum mass of 17.8 $M_{\oplus}$ and an orbital period of 45.8 days. The corresponding RV signal is not evident in the BFPs for the activity indices of *S*-index and Hα shown in Figure 12.
10. *HD 8326* is a K star with a mass of 0.8 $M_{\odot}$ and a distance of 30.71 pc. The candidate is consistent with a planet with a minimum mass of 66.4 $M_{\oplus}$ and an orbital period of 159 days, which is consistent with the temperate zone around this star. The corresponding RV signal is not evident in the BFPs for the activity indices of the *S*-index and Hα shown in Figure 13.

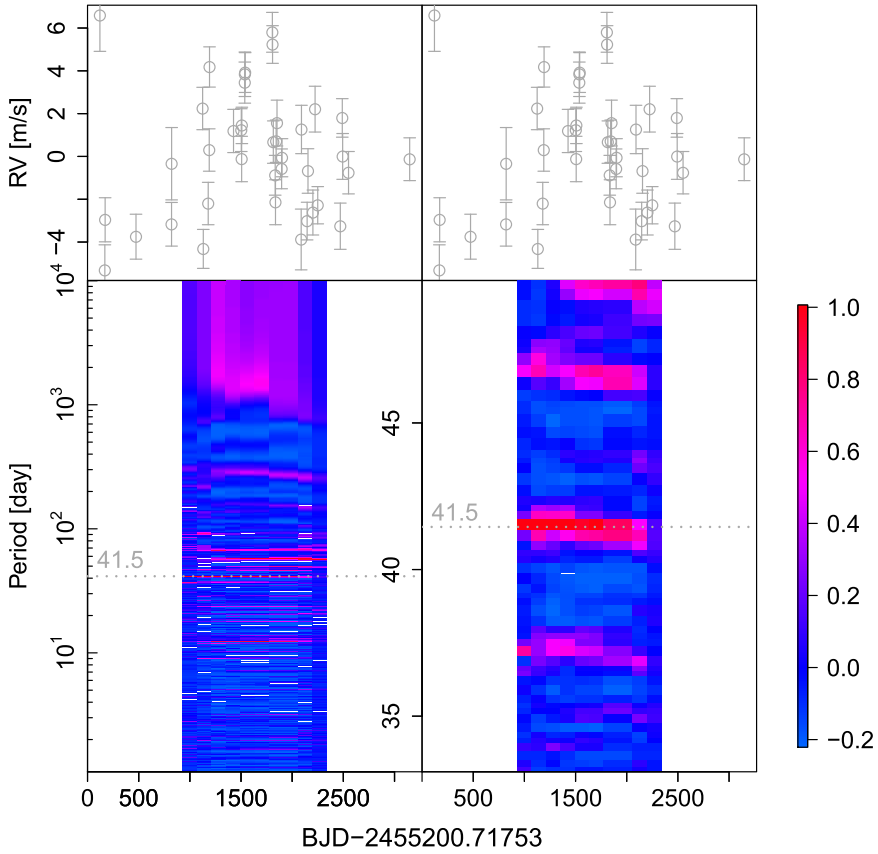

Figure 7. Moving periodogram for HIP 35173 b. The window size is 2000 days and the number of steps is 10. The other signals in the bottom right panel are the annual aliases of the 41.5-day signal.

11. *HD 164604* is a K star with a mass of 0.77 $M_{\odot}$ and a distance of 39.41 pc. The candidate is consistent with a Jupiter with a minimum mass of 635 $M_{\oplus}$ and an orbital period of 641 days. The corresponding RV signal is not evident in the BFPs for the activity indices of the *S*-index and Hα shown in Figure 14.
12. *HIP 54373* is a K star with a mass of 0.57 $M_{\odot}$ and a distance of 18.73 pc. There are two-planet candidates corresponding to (1) a hot super-Earth with a minimum mass of 8.6 $M_{\oplus}$ and an orbital period of 7.76 days and (2) a hot Neptune with a minimum mass of 12.4 $M_{\oplus}$ and an orbital period of 15.1 days. The orbits of these two planets form a 1:2 resonance. The eccentricities of these two candidate planets are consistent with zero since $e = 0$ is less than 2σ away from the means. The corresponding two RV signals are consistently identified in the BFPs for various noise models (see P5, P6, P8, P9, P11, and P12 in Figure 15) and do not show significant power excess in the BFPs for the *S*-index and Hα. They are also consistent in time, as seen from the moving periodograms shown in Figures 16 and 17. The two-planet solution is favored over the one-planet solution because ln(BF) = 5.2. The MAP value of the eccentricity for the 15.1 days signal decreases from 0.30 for the one-planet model to 0.24 for the two-planet model. Thus, the 7.76 days signal is favored by the data in terms of increasing the goodness of fit and reducing the eccentricity of the 15.1 days signal to a lower and, thus, more reasonable value (Kipping 2013). According to our analysis of the RV data, there are potentially additional signals, which warrants further observations and analyses.
13. *HD 24085* is a G star with a mass of 1.22 $M_{\odot}$ and a distance of 54.99 pc. The planet candidate is consistent with a hot Neptune with a minimum mass of 11.8 $M_{\oplus}$ and an orbital period of 2.04 days. The corresponding RV signal is not evident in the BFPs for the activity indices of the *S*-index and Hα shown in Figure 18.
14. *HIP 71135* is an M star with a mass of 0.66 $M_{\odot}$ and a distance of 32.36 pc. The planet candidate is consistent with a Neptune with a minimum mass of 18.8 $M_{\oplus}$ and an orbital period of 87.2 days, which is consistent with the temperate zone around this star. The corresponding RV signal is not evident in the BFPs for the activity indices of the *S*-index and Hα shown in Figure 19. The signal is consistent in time, as seen from the moving periodogram shown in Figure 20.

5. Conclusion

We introduce a procedure to diagnose the nature of signals in RV data. In this diagnosis framework, we confirm a signal as Keplerian if it is statistically significant, consistent in time, robust in the choice of noise models, and not correlated with stellar activity. We develop an automated algorithm to implement this procedure. The application of this algorithm

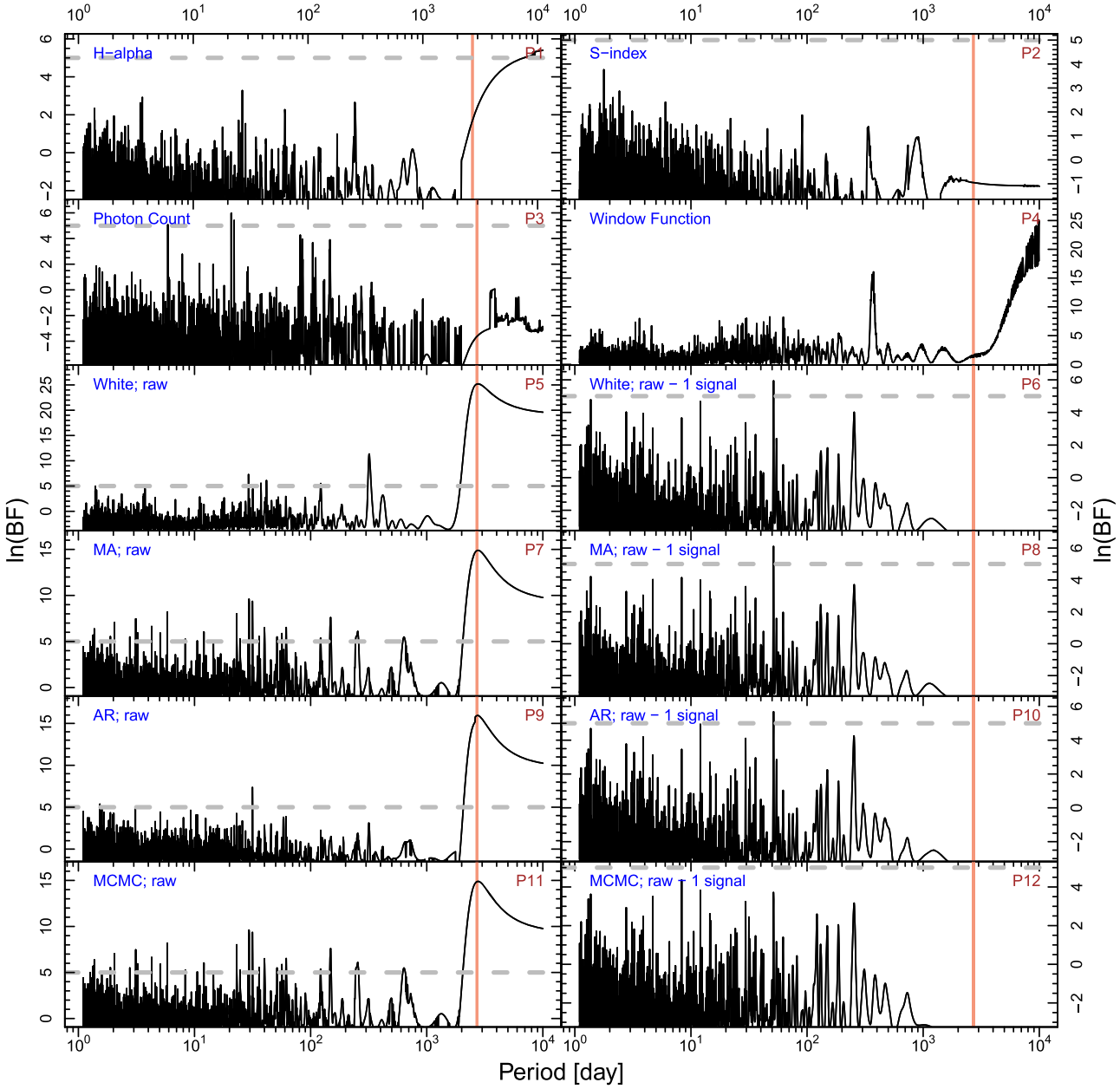

Figure 8. BFPs for HD 102843. The red line shows the signal at a period of about 3000 days.

to the PFS data leads to an initial identification of about 200 primordial signals of high quality.

We report 15 planet candidates from these primordial signals based on analyses of 14 PFS RV data sets that are obtained for six G stars, seven K stars, and one M star. The masses of planets vary from $8\,M_{\oplus}$ to $153\,M_{\oplus}$, and the RV semi-amplitudes vary from 1.7 to $12\,\mathrm{m\,s^{-1}}$. The detections of these signals demonstrate the ability of PFS to discover small planets around nearby stars.

In particular, we report candidates HD 210193 b, HD 103949 b, HD 8326 b, and HIP 71135 b, which are located in the temperate zones of their stellar hosts and could potentially host temperate moons. We also report candidates HIP 54373 b and c, which form a 1:2 resonance. Such a resonance can stabilize a multiple-planet system for a long period of time, as was discovered in the TRAPPIST-1 system (Gillon et al. 2016; Luger et al. 2017).

Because our algorithm only automatically identifies signals in RV data obtained by a single instrument, we choose to report the signals for targets without other RV data sets available. Thus, we do not check the consistency between PFS and other instruments. An updated algorithm will be developed to automatically analyze multiple RV data sets and to identify potential signals efficiently. Such an algorithm is suitable for modern RV surveys, such as PFS, the High Accuracy Radial Velocity Planet Searcher (HARPS; Pepe et al. 2002), and the Automated Planet Finder (APF; Vogt et al. 2014). Our algorithm also provides a diagnostic framework for reliable detections of exoplanets using the RV method.

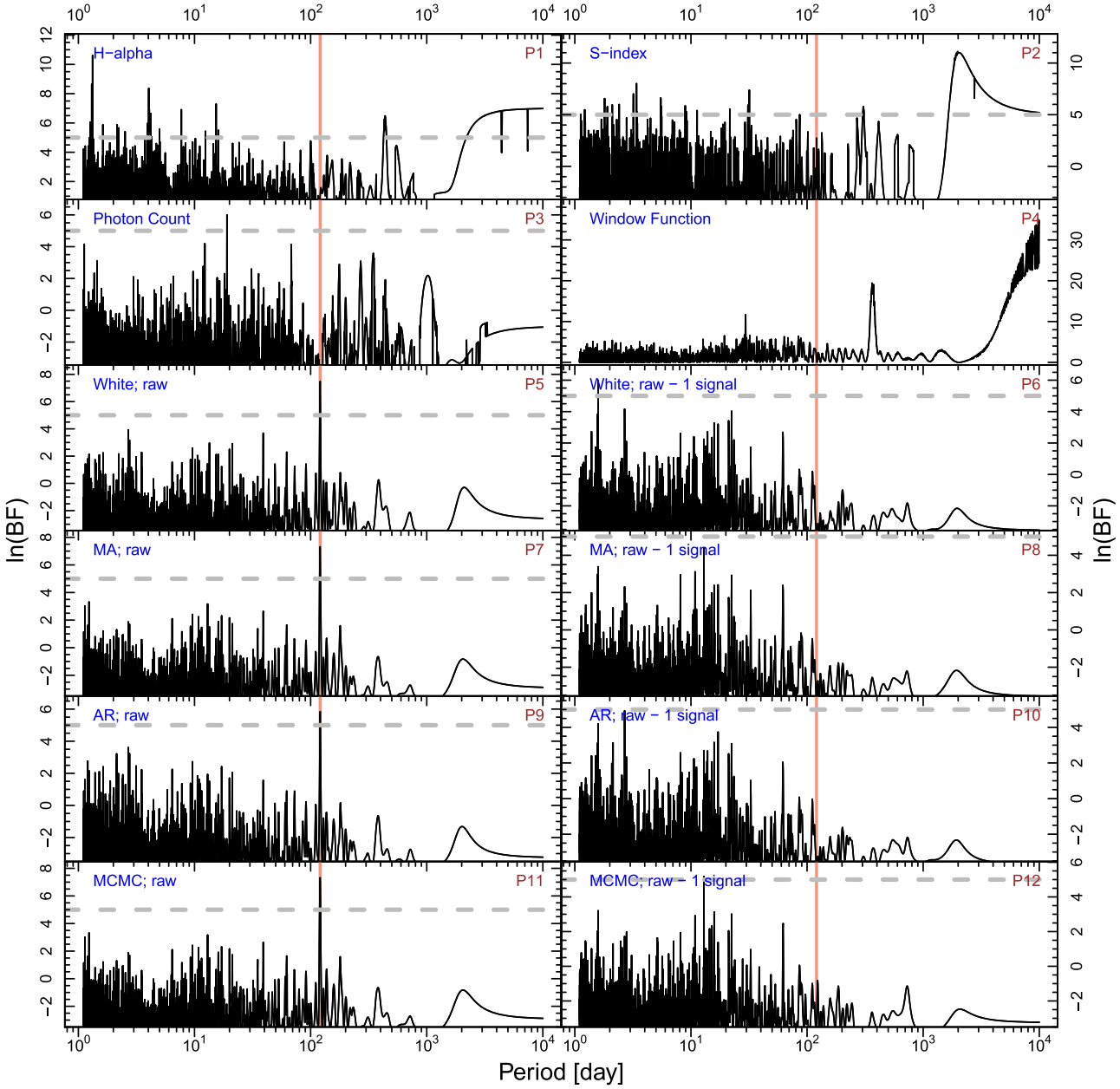

Figure 9. BFPs for HD 103949. The red line shows the signal at a period of 121 days.

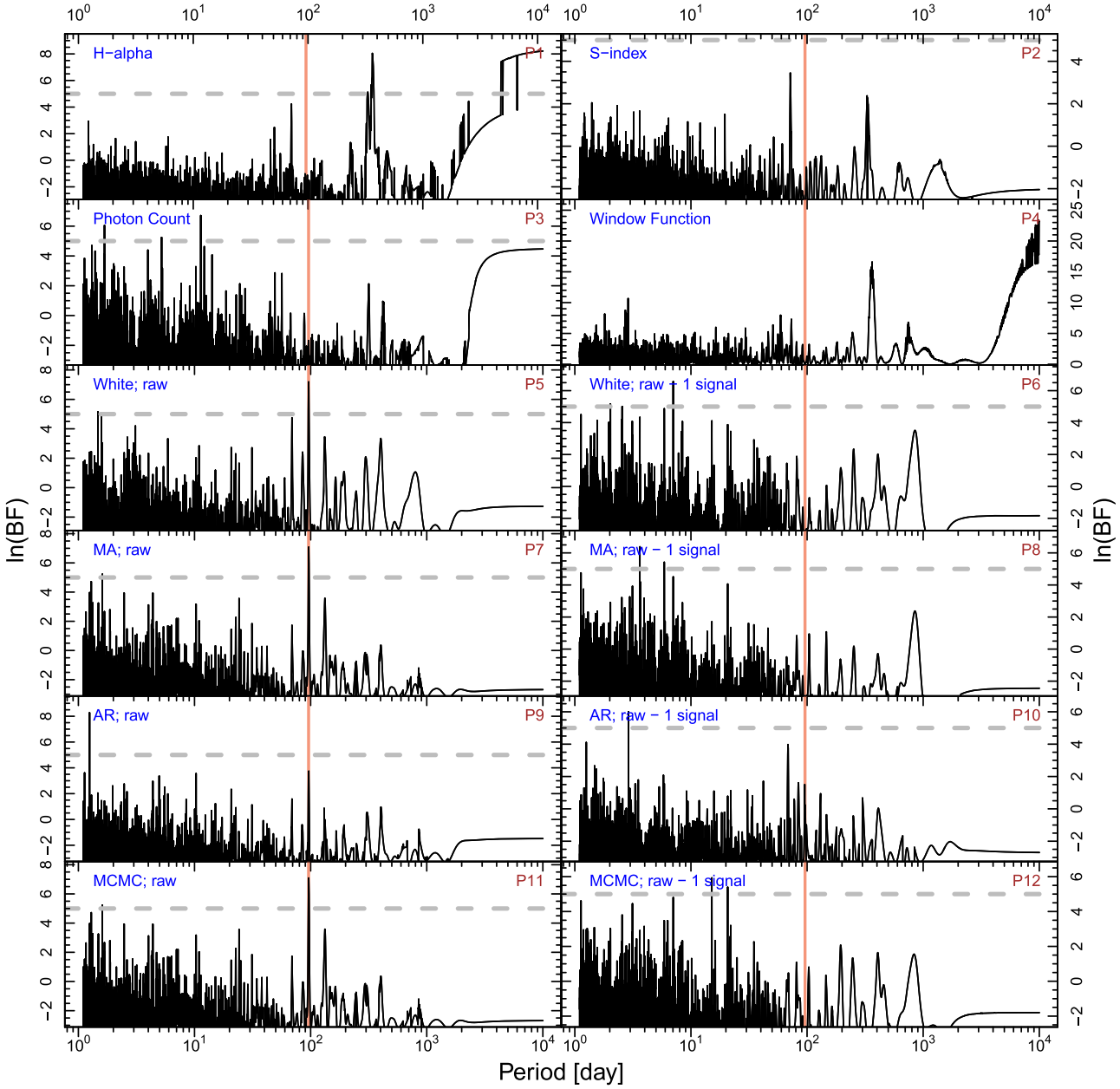

Figure 10. BFPs for HD 206255. The red line shows the signal at a period of 96.0 days.

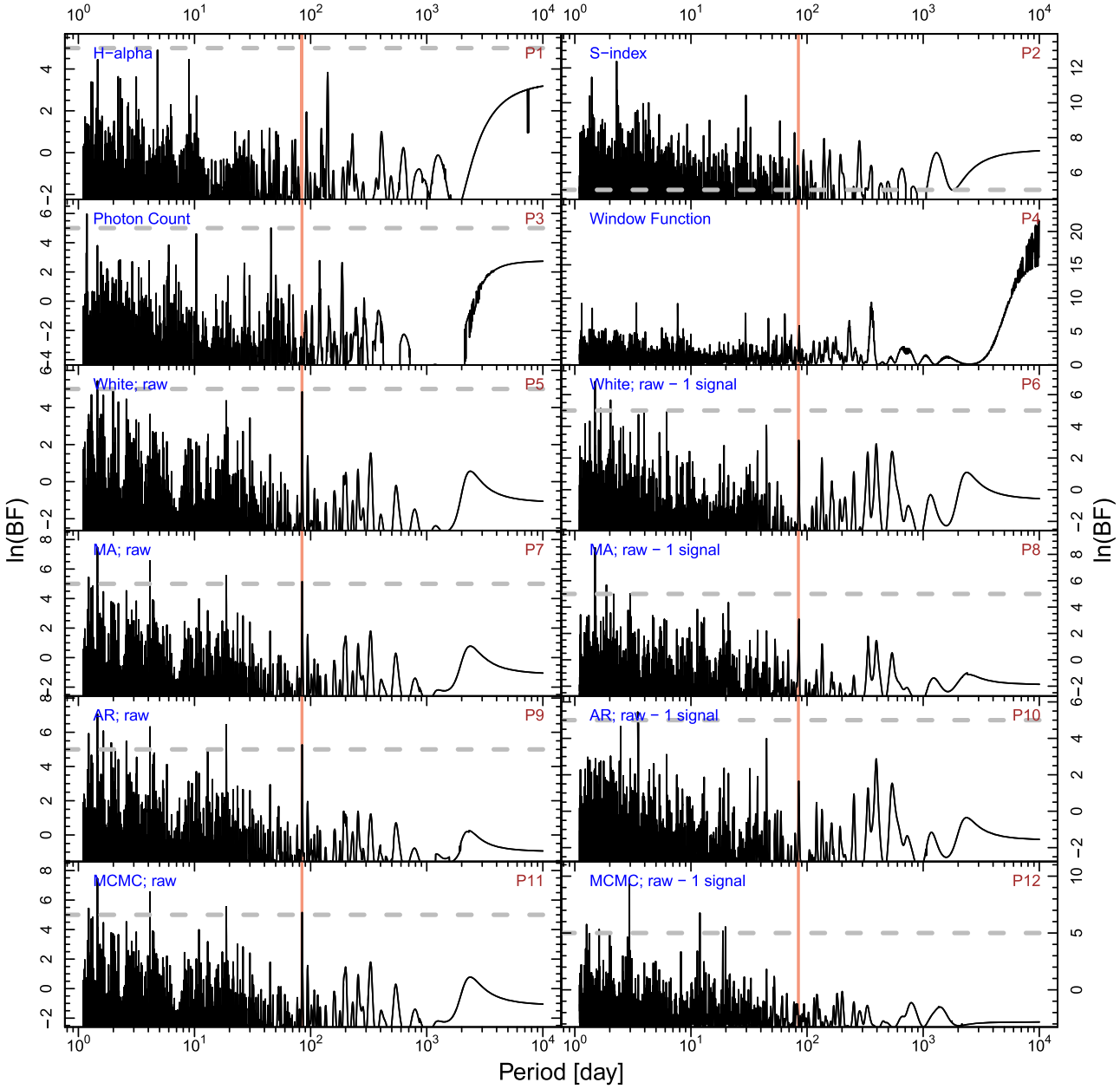

Figure 11. BFPs for HD 21411. The red line shows the signal at a period of 84.3 days.

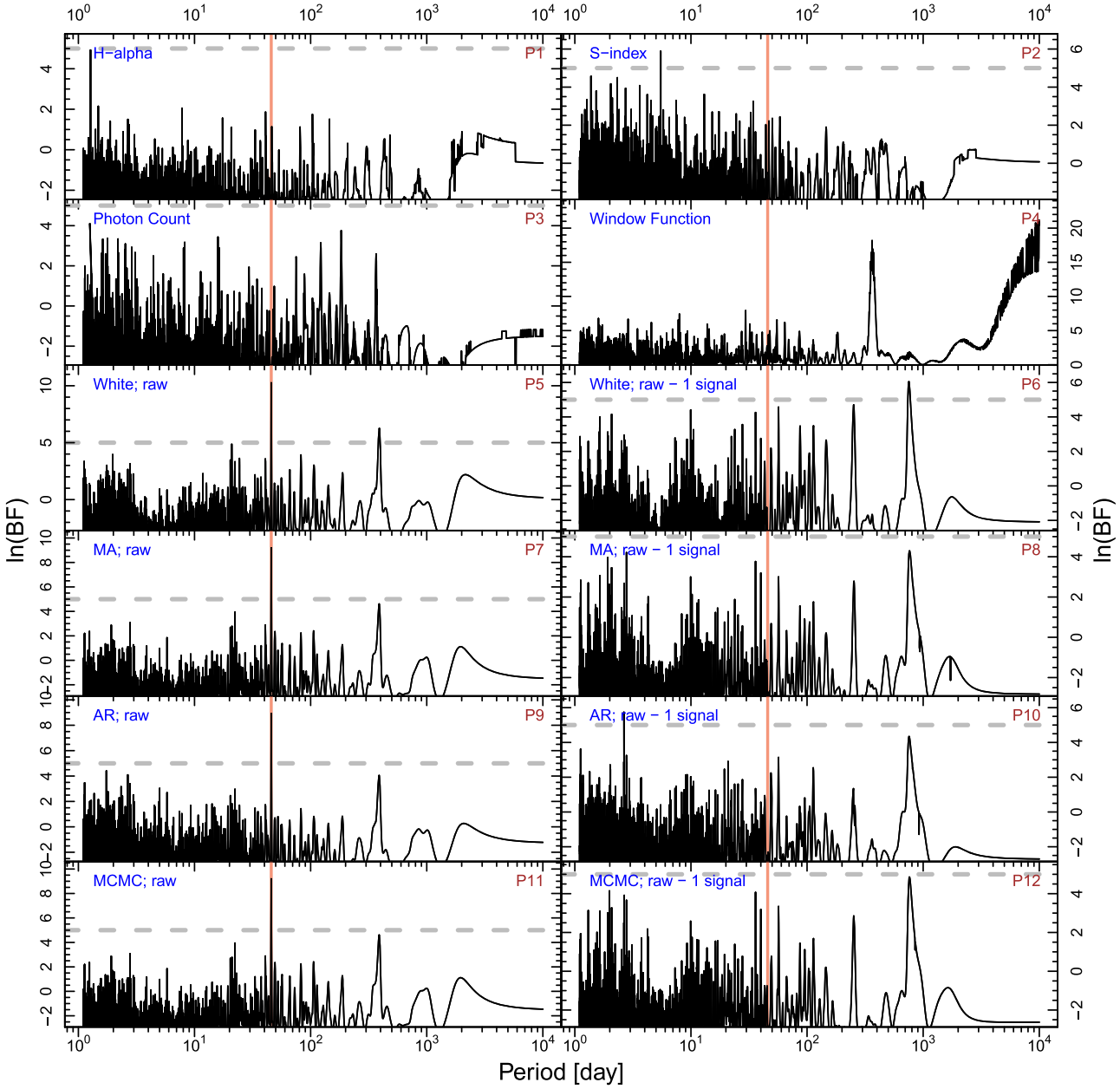

Figure 12. BFPs for HD 64114. The red line shows the signal at a period of 45.8 days.

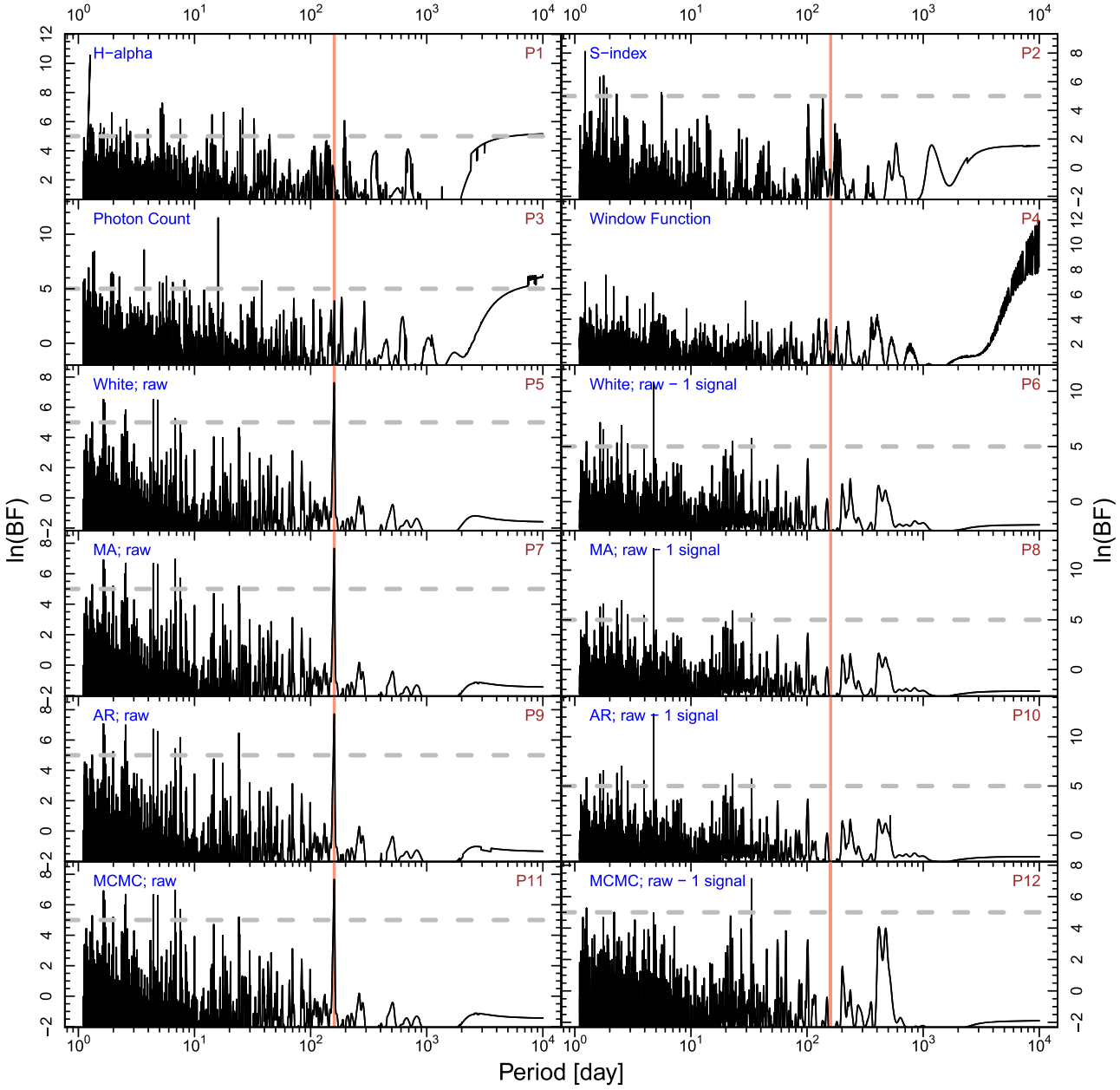

Figure 13. BFPs for HD 8326. The red line shows the signal at a period of 159 days.

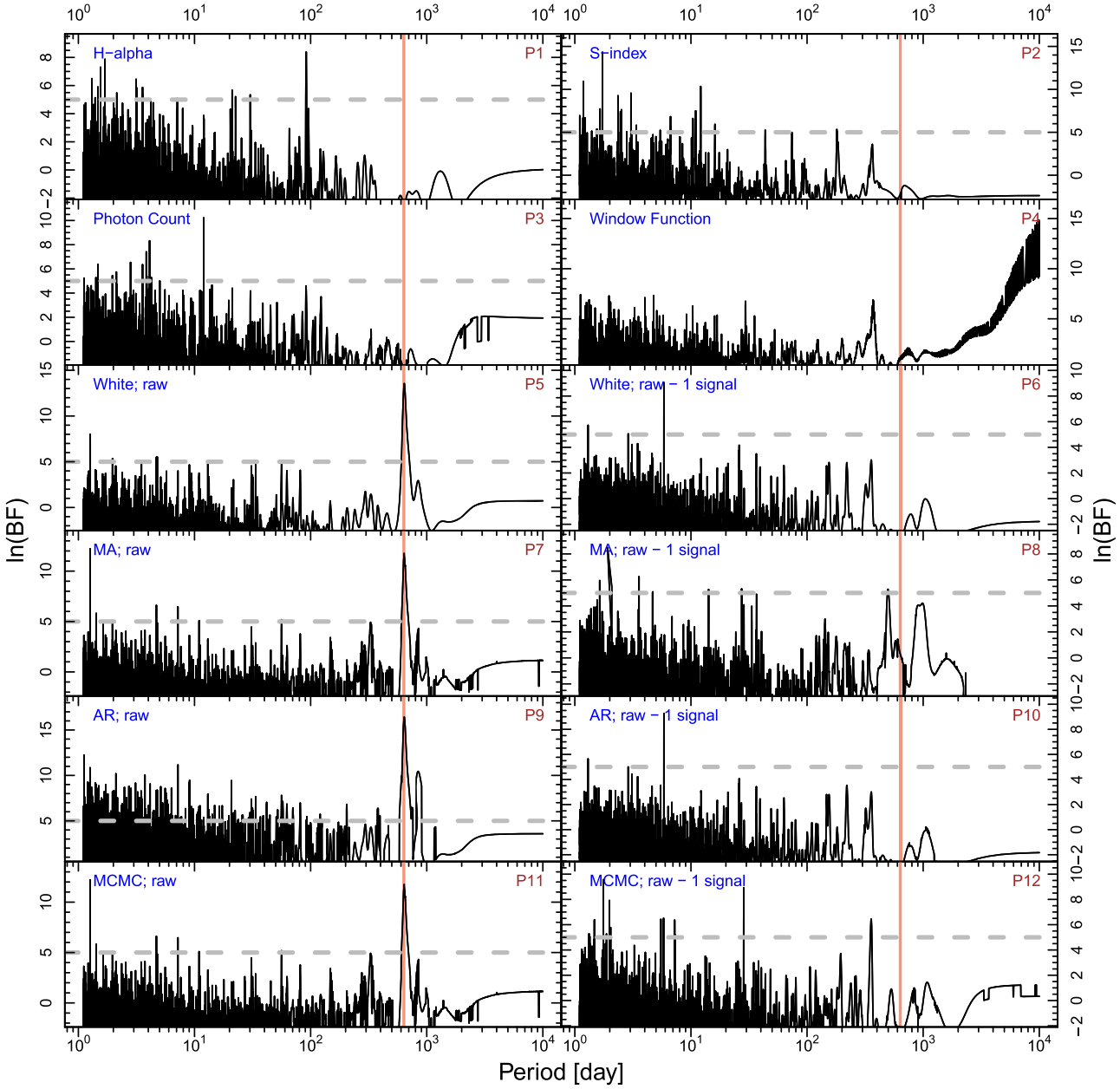

Figure 14. BFPs for HD 164604. The red line shows the signal at a period of 635 days.

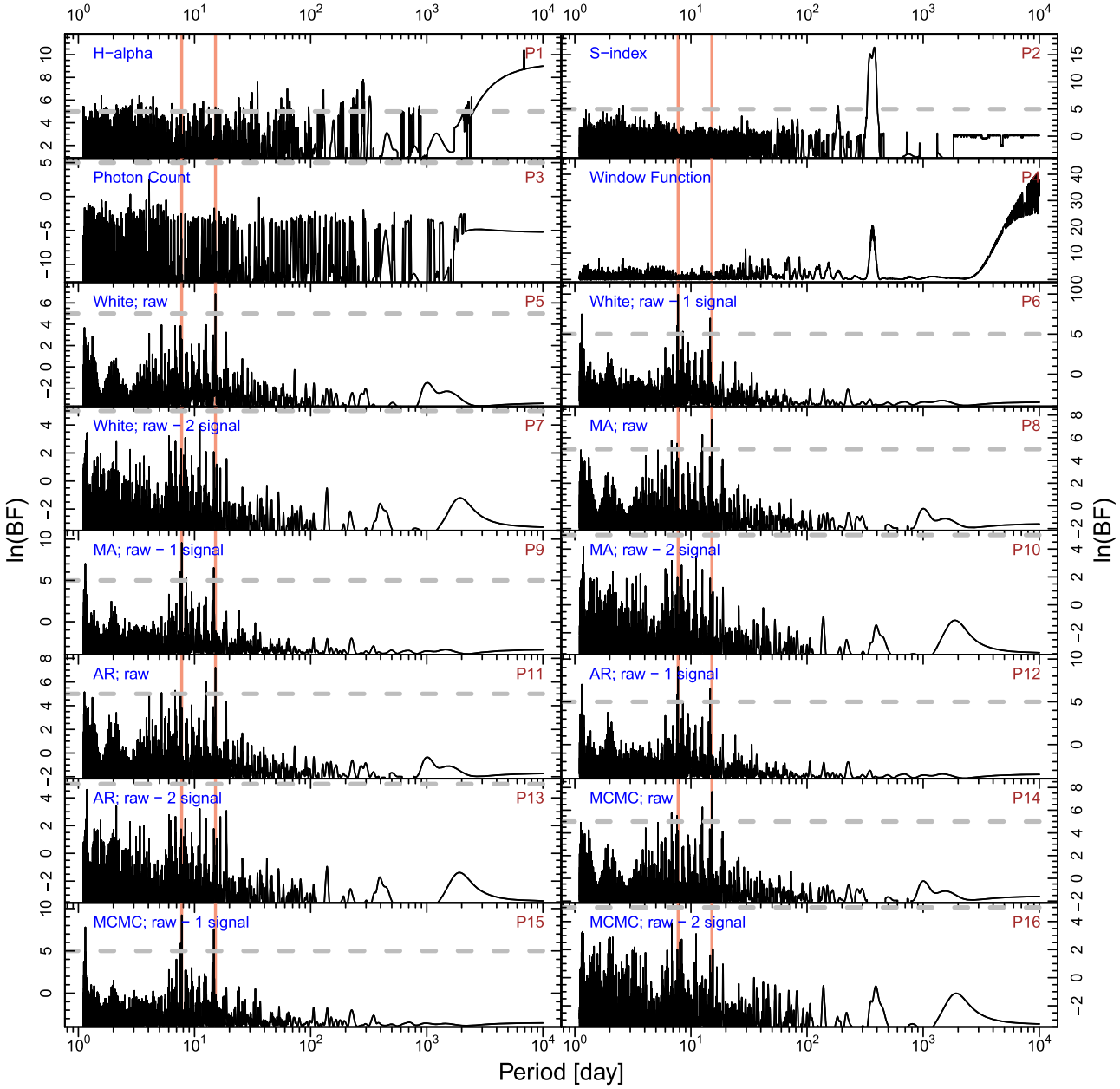

Figure 15. BFPs for HIP 54373. The red lines show the signals at periods of 15.1 and 7.76 days.

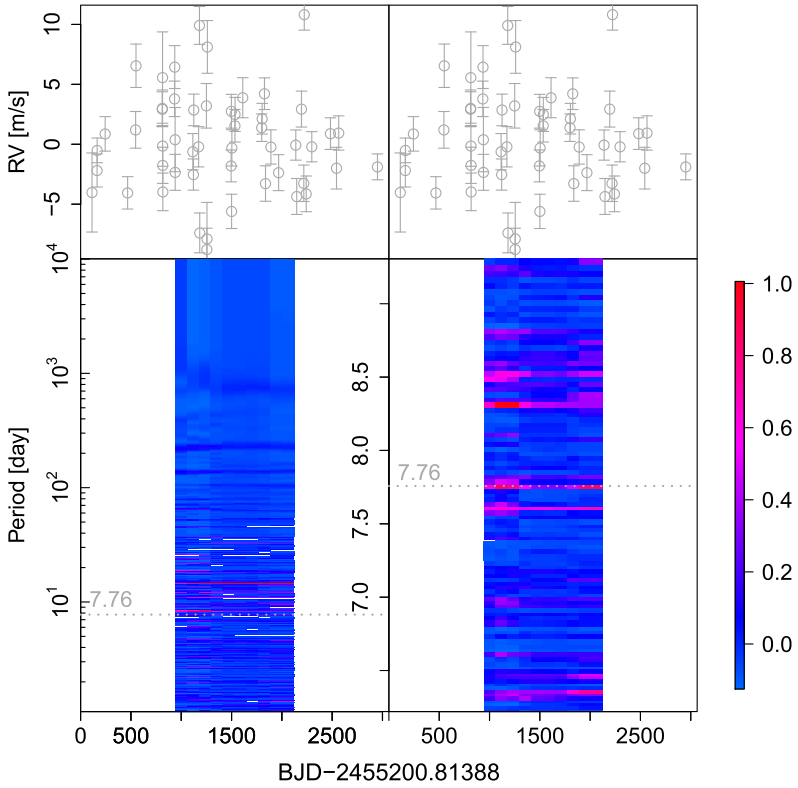

Figure 16. Moving periodogram for HIP 54373 b. The window size is 2000 days and the number of steps is 10. The signal near the 7.76-day signal is its annual alias.

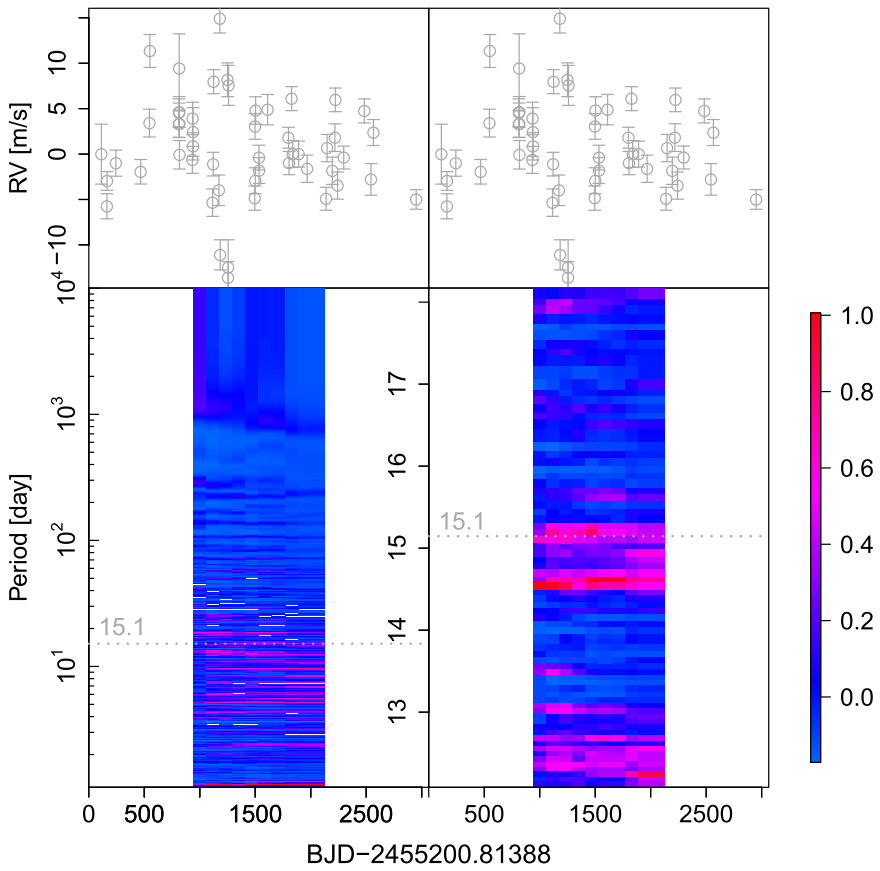

Figure 17. Moving periodogram for HIP 54373c. The window size is 2000 days and the number of steps is 10. The signal near the 15.1-day signal is its annual alias.

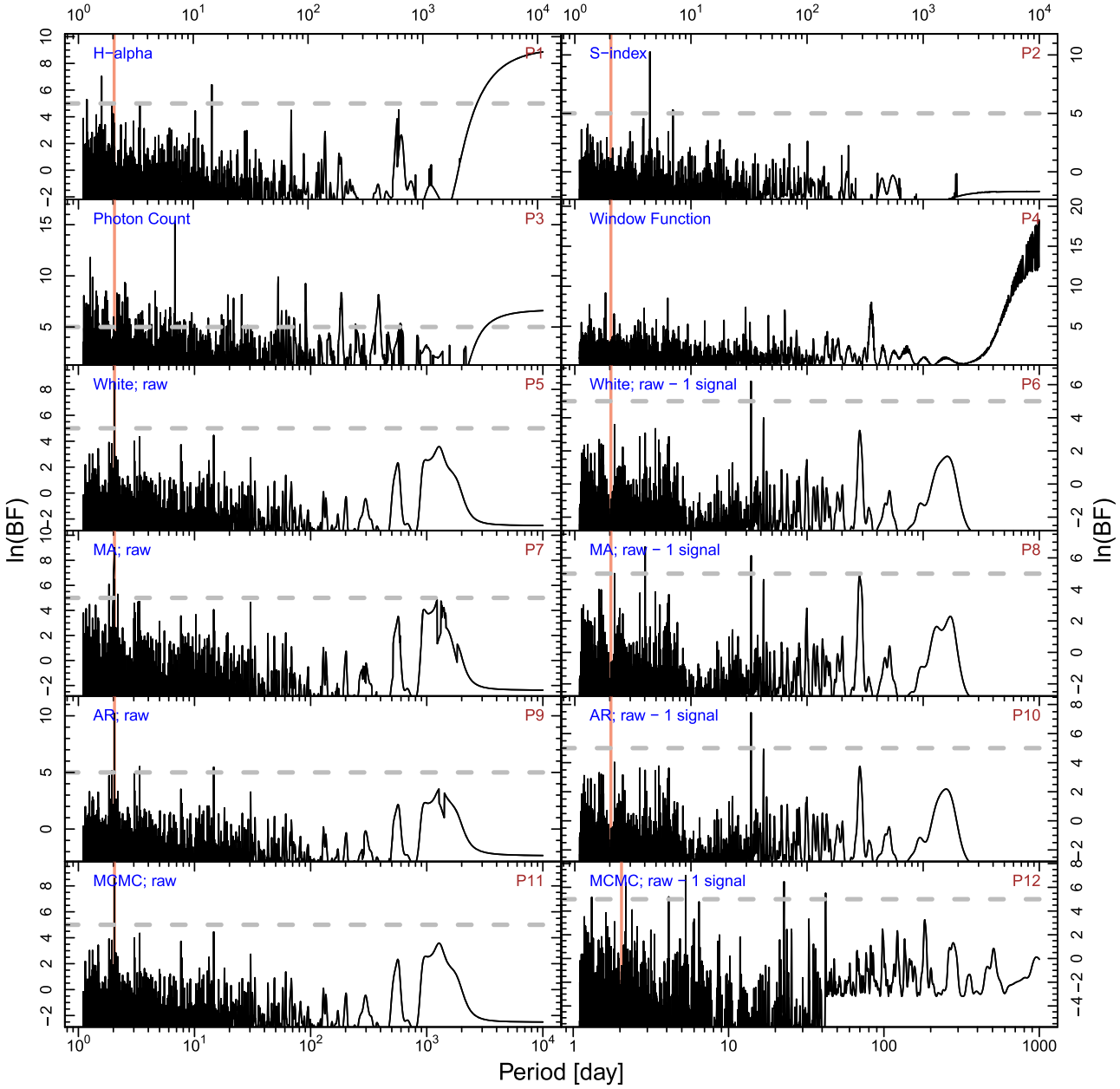

Figure 18. BFPs for HD 24085. The red line shows the signal at a period of 2.05 days.

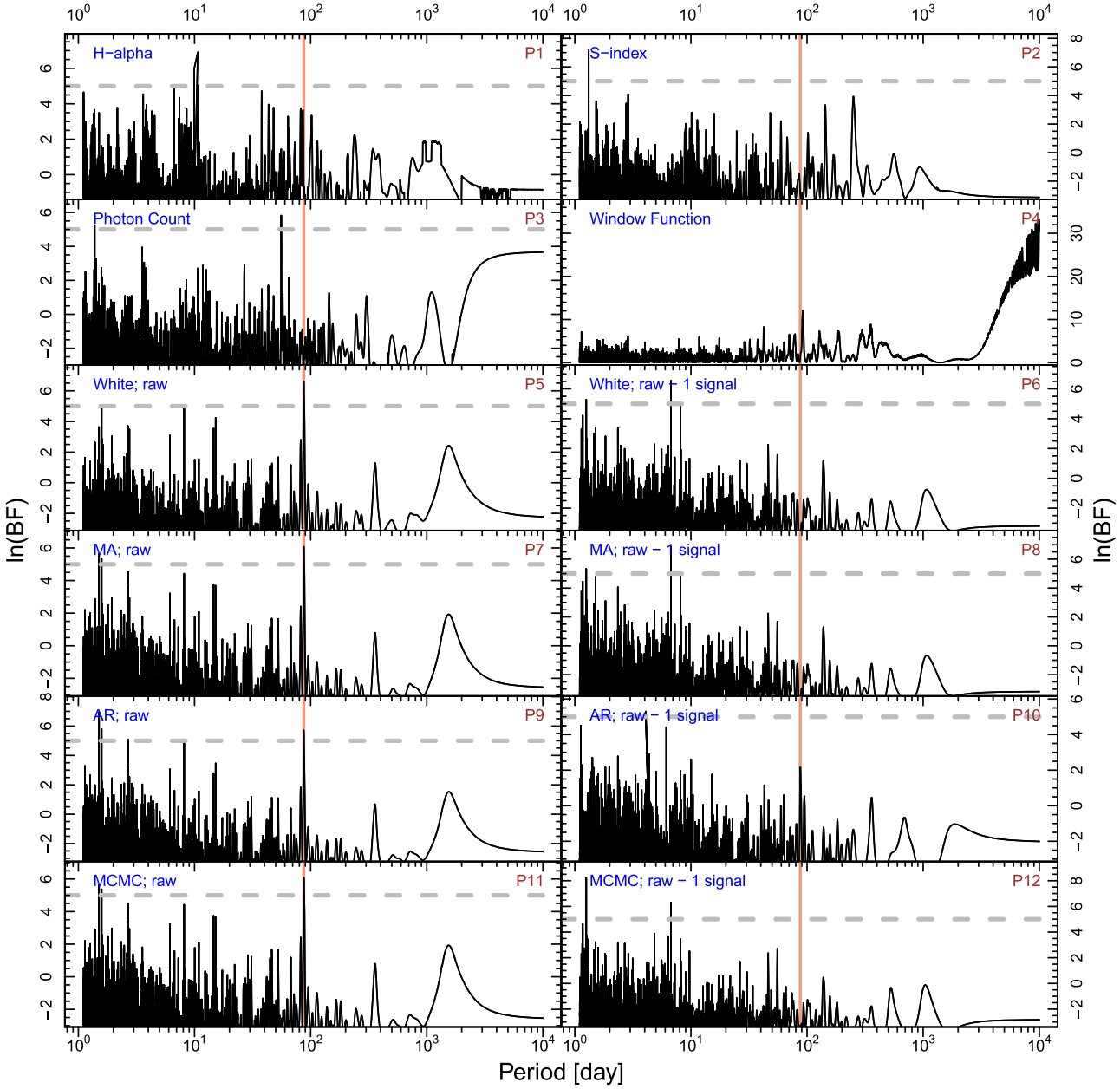

Figure 19. BFPs for HIP 71135. The red line shows the signal at a period of 87.2 days.

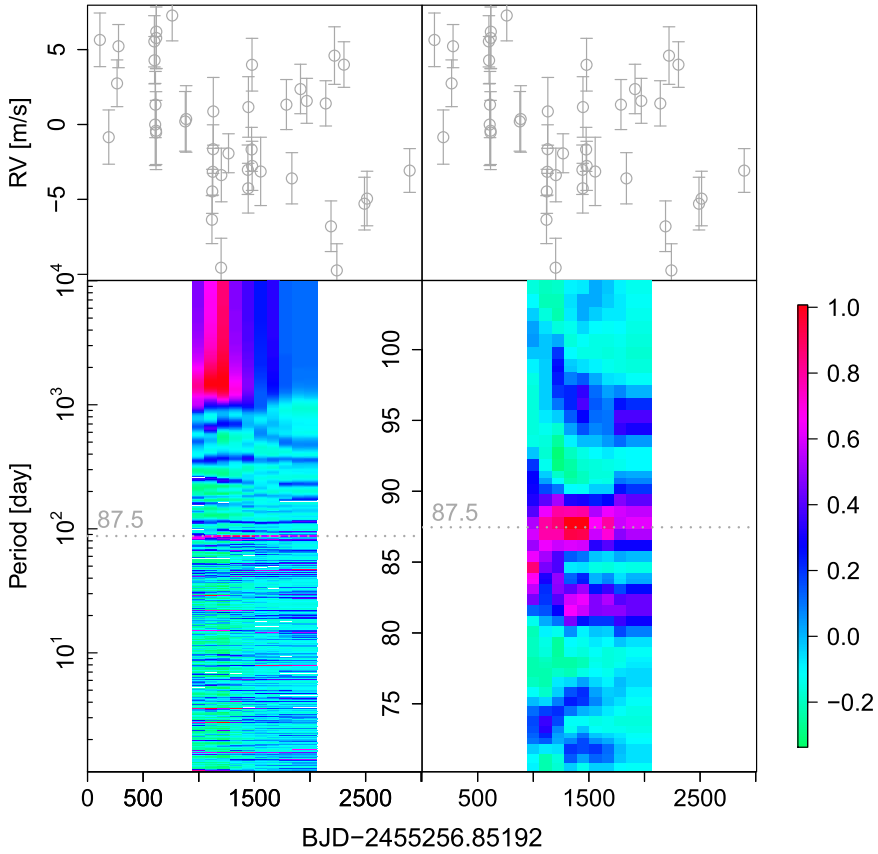

Figure 20. Moving periodogram for HIP 71135 b. The window size is 2000 days and the number of steps is 10. The annual alias of 87.5-day signal also shows excess power in the bottom right panel.

This work has made use of data from the European Space Agency (ESA) mission *Gaia* (https://www.cosmos.esa.int/gaia), processed by the *Gaia* Data Processing and Analysis Consortium (DPAC, https://www.cosmos.esa.int/web/gaia/dpac/consortium). Funding for the DPAC has been provided by national institutions, in particular the institutions participating in the *Gaia* Multilateral Agreement. Support for this work was provided by NASA through Hubble Fellowship grant *HST*-HF2-51399.001 awarded by the Space Telescope Science Institute, which is operated by the Association of Universities for Research in Astronomy, Inc., for NASA, under contract NAS5-26555. The authors acknowledge the years of technical support from LCO staff in the successful operation of PFS, enabling the collection of the data presented in this paper.

Software: R package magicaxis (Robotham 2016), fields (Nychka et al. 2018), minpack.lm (Elzhov et al. 2016).

ORCID iDs

Fabo Feng https://orcid.org/0000-0001-6039-0555
Jeffrey D. Crane https://orcid.org/0000-0002-5226-787X
R. Paul Butler https://orcid.org/0000-0003-1305-3761

References

Anglada-Escudé, G., Amado, P. J., Barnes, J., et al. 2016, Natur, 536, 437
Anglada-Escudé, G., Tuomi, M., Gerlach, E., et al. 2013, A&A, 556, A126
Astudillo-Defru, N., Forveille, T., Bonfils, X., et al. 2017, A&A, 602, A88
Benedict, G., Henry, T., Franz, O., et al. 2016, AJ, 152, 141
Butler, R. P., Marcy, G. W., Williams, E., et al. 1996, PASP, 108, 500
Crane, J. D., Shectman, S. A., Butler, R. P., et al. 2010, Proc. SPIE, 7735, 773553
Dumusque, X. 2016, A&A, 593, A5
Dumusque, X. 2018, A&A, 620, A47
Eker, Z., Soydugan, F., Soydugan, E., et al. 2015, AJ, 149, 131
Elzhov, T. V., Mullen, K. M., Spiess, A.-N., et al. 2016, minpack.lm: R Interface to the Levenberg-Marquardt Nonlinear Least-Squares Algorithm Found in MINPACK, Plus Support for Bounds, https://cran.r-project.org/web/packages/minpack.lm/index.html
Feng, F., Tuomi, M., & Jones, H. R. A. 2017a, MNRAS, 470, 4794
Feng, F., Tuomi, M., Jones, H. R. A., et al. 2017b, AJ, 154, 135
Feng, F., Tuomi, M., Jones, H. R. A., Butler, R. P., & Vogt, S. 2016, MNRAS, 461, 2440
Fischer, D., Anglada-Escude, G., Arriagada, P., et al. 2016, PASP, 128, 964
Gaia Collaboration, Brown, A. G. A., Vallenari, A., et al. 2018, A&A, 616, 1
Gillon, M., Jehin, E., Lederer, S. M., et al. 2016, Natur, 533, 221
Gregory, P. C. 2011, MNRAS, 410, 94
Haario, H., Laine, M., Mira, A., & Saksman, E. 2006, Stat. Comput., 16, 339
Haywood, R., Collier Cameron, A., Queloz, D., et al. 2014, MNRAS, 443, 2517
Kane, S. R., Ciardi, D. R., Gelino, D. M., & von Braun, K. 2012, MNRAS, 425, 757
Kass, R. E., & Raftery, A. E. 1995, J. Am. Stat. Assoc., 90, 773
Kipping, D. M. 2013, MNRAS, 434, L51
Kopparapu, R. K., Ramirez, R. M., SchottelKotte, J., et al. 2014, ApJL, 787, L29
Lomb, N. R. 1976, Ap&SS, 39, 447
Luger, R., Sestovic, M., Kruse, E., et al. 2017, NatAs, 1, 0129
Malkov, O. Y. 2007, MNRAS, 382, 1073
Marcy, G. W., & Butler, R. P. 1992, PASP, 104, 270
Mayor, M., Lovis, C., & Santos, N. C. 2014, Natur, 513, 328
Nychka, D., Furrer, R., Paige, J., Sain, S., & Nychka, M. D. 2018, fields: Tools for Spatial Data, https://cran.r-project.org/web/packages/fields/index.html
Pepe, F., Mayor, M., Rupprecht, G., et al. 2002, Msngr, 110, 9
Pepe, F. A., Cristiani, S., Rebolo Lopez, R., et al. 2010, Proc. SPIE, 7735, 77350F
Raftery, A. E. 1995, Sociological Method., 25, 111
Rajpaul, V., Aigrain, S., Osborne, M. A., Reece, S., & Roberts, S. 2015, MNRAS, 452, 2269

Ribas, I., Tuomi, M., Reiners, A., et al. 2018, Natur, 563, 365
Ricker, G. R., Winn, J. N., Vanderspek, R., et al. 2014, JATIS, 1, 014003
Robotham, A. S. G. 2016, magicaxis: Pretty Scientific Plotting with Minor-tick and Log Minor-tick Support, Astrophysics Source Code Library, ascl:1604.004
Scargle, J. D. 1982, ApJ, 263, 835
Schwab, C., Rakich, A., Gong, Q., et al. 2016, Proc. SPIE, 9908, 99087H
Teske, J. K., Wang, S., Wolfgang, A., et al. 2018, AJ, 155, 148
Tuomi, M., & Anglada-Escudé, G. 2013, A&A, 556, A111
Tuomi, M., Jones, H. R. A., Jenkins, J. S., et al. 2013, A&A, 551, A79
Van Eylen, V., Albrecht, S., Huang, X., et al. 2019, AJ, 157, 61
Vogt, S. S., Radovan, M., Kibrick, R., et al. 2014, PASP, 126, 359
Wenger, M., Ochsenbein, F., Egret, D., et al. 2000, A&AS, 143, 9